Università degli Studi di Napoli “Federico II”

SCUOLA POLITECNICA E DELLE SCIENZE DI BASE

DIPARTIMENTO DI INGEGNERIA INDUSTRIALE

CORSO DI LAUREA IN INGEGNERIA AEROSPAZIALE

CLASSE DELLE LAUREE IN INGEGNERIA INDUSTRIALE (L-9)

Elaborato di laurea in Meccanica del Volo

Geometric modelling, stability and control analysis of the asymmetric Rutan Boomerang aircraft

Relatore:
Prof. Danilo Ciliberti

Candidato:
Rester Brendon Entienza
Matr. N35004277

ANNO ACCADEMICO 2023 – 2024

To
my love
Krizzia,
my loving mother Raissa and my hardworking father Brendo,
without whom none of this would have been possible.
To my
siblings
Raiven,
Rovic,
and
my
dog
Althea.
To my nanay Ester and my aunt Kelly,
who are my caring second mothers.

Abstract

The purpose of this thesis is to create a geometric 3D model of the asymmetric Rutan Boomerang and to conduct a preliminary study regarding its stability and control. The analysis also considers propulsive effects, specifically the impact of asymmetric thrust. At last, a quick comparison with a symmetric aircraft has been made. For this thesis, the Boomerang was chosen due to its interesting and unconventional design, in particular, this work attempts to answer the question: "*can that airplane fly straight*?" The design was developed without wind tunnel testing or advanced computational tools, hence this work proposes to address the latter gap. NASA's Open Vehicle Sketch Pad (VSP) is used for geometric modeling, and aerodynamic analysis was performed using the VSPAERO tool, specifically through the vortex lattice method (VLM). Additionally, MATLAB and Microsoft Excel have been used to produce charts, plots and slope estimates. Due to the limitations of the chosen method, the results require further validation through wind tunnel testing or more advanced CFD tools. Nonetheless, this study shows that software like Open VSP, can be effectively and swiftly used to develop and evaluate both conventional and innovative aircraft designs.

Sommario

Lo scopo di questa tesi è di creare un modello geometrico 3D del velivolo asimmetrico Rutan Boomerang, e di condurre uno studio preliminare sulla stabilità e controllo. L'analisi considera anche gli effetti propulsivi, in particolare, l'impatto della spinta asimmetrica. Infine, un confronto con un velivolo simmetrico è stato fatto. Per questo elaborato, il Boomerang è stato scelto per il suo design unico e non convenzionale, in particolare questo elaborato cerca di rispondere alla domanda: "*può quell'aereo volare dritto?"* Il progetto è stato sviluppato senza alcuna prova in galleria del vento né con l'utilizzo di strumenti computazionali avanzati; dunque, questo lavoro si propone di colmare quest'ultima lacuna. Il software Open VSP della NASA è stato utilizzato per la modellazione geometrica, mentre le analisi aerodinamiche sono state condotte tramite lo strumento VSPAERO, nello specifico, con il metodo vortex lattice (VLM). Inoltre, MATLAB e Microsoft Excel sono stati utilizzati per generare tabelle, grafici e stime di pendenze. A causa delle limitazioni del metodo scelto, i dati prodotti dall'analisi richiedono ulteriori validazioni tramite prove in galleria del vento o l'utilizzo di strumenti CFD più avanzati. Tuttavia, questo studio dimostra che software come Open VSP possono essere usati in modo efficace e rapido per creare e valutare design convenzionali e non.

Table of contents

List of figures

List of tables

1. Introduction

1.1 Objectives

This thesis aims to perform geometric modeling of the Rutan Boomerang using NASA's Open Vehicle Sketch Pad (Open VSP) and conduct preliminary aerodynamic analysis through the Vortex Lattice Method (VLM) using VSPAERO, focusing on evaluating the aircraft's longitudinal and lateral-directional stability and control. Propulsive effects are also analyzed, with a major interest in the effects of asymmetric thrust. Finally, the values yielded by the analysis are juxtaposed to those of a symmetric light twin-engine aircraft.

1.2 Work layout

Chapter 1: Assesses the thesis' purpose, presents Rutan Boomerang aircraft, the software and the method used for the analysis.

Chapter 2: Exhibits the process of geometric modelling and meshing of the aircraft of interest, component by component with Open VSP.

Chapter 3: Presents and discusses the aerodynamic analysis results of the aircraft's longitudinal stability and control characteristics, with some comments on coupling effects.

Chapter 4: Same as chapter three, but for the aircraft's lateral-directional stability and control.

Chapter 5: Focuses on the propulsive effects, with a major interest in asymmetric thrust.

Chapter 6: Compares the aerodynamic characteristics of the Rutan Boomerang with those of a symmetric twin-engine aircraft.

1.3 Burt Rutan’s Boomerang

Figure 1.1 - Rutan Boomerang

The Rutan Boomerang, designed by Burt Rutan, is a one-of-a-kind experimental asymmetric aircraft that addresses the challenges of asymmetrical thrust in twin-engine aircraft. Its asymmetric configuration is a departure from conventional designs, focusing on enhanced control, safety, and efficiency.

1.3.1 Asymmetrical Design and Stability

In traditional twin-engine aircraft, engines positioned far from the centerline create significant yawing moments during engine failure, complicating control and stability. Rutan mitigated this issue by moving the right engine closer to the fuselage, positioning both engines near the aircraft’s center of gravity. This adjustment reduces asymmetrical thrust effects and drag by minimizing the frontal area compared to traditional configurations. The designer further refined the airframe to ensure stability and control, allowing consistent performance during single-engine operation. Additional refinements include the left engine being slightly offset from the effective centerline to align thrust lines during high angles of attack, addressing P-factor challenges. These measures ensure superior control and safety.

1.3.2 Single-Engine Performance

The Boomerang exhibits outstanding single-engine performance. It maintains full operational control without requiring rudder input, even at full power. Its forward-swept wing design ensures that wing roots stall before the tips, preserving roll control during stalls. When stalling, the aircraft naturally lowers its nose, increases air speed, and regains stable flight. Even under prolonged stall conditions, the Boomerang retains directional control, enabling repeated stall and recovery cycles. In contrast, conventional twin-engine aircraft often lose control due to excessive asymmetrical thrust, even with full rudder deflection.

1.3.3 Aerodynamic Features

The wing features full-span ailerons that double as flaperons, enhancing control and versatility. These ailerons can deflect upward for camber control, improving aerodynamic efficiency at high speeds. Additionally, the Boomerang's dual-tail configuration, located within the engines' prop wash, enhances yaw control and stability, particularly during low-speed operations or engine-out scenarios.

1.3.4 Legacy and Achievement

Despite its unconventional appearance, the Boomerang represents Burt Rutan's greatest contribution to general aviation. It achieves exceptional efficiency and practicality while eliminating the risks associated with asymmetrical thrust. Remarkably, the design was developed without wind tunnel testing or advanced computational tools, underscoring Rutan's ingenuity and expertise. The Boomerang remains a symbol of experimental aviation's potential to redefine established norms.

Boomerang Model 202-11

- Engines = Left - Lyc TIO-360A1B 200HP / Right - Lyc TIO-360C1A6D 210HP
- Span=36.7 ft Length=30.6 ft Wing Area=101.7 Sqft
- Weight Empty = 2370 lb
- Max Gross Weight = 4242 lb
- Max Climb = 1900 fpm (2900 fpm @ 2800 lb)
- Stall Speed =88 Kt at 4200lb or 73 Kt @ 2800 lb
- Vmax = 283 Knots True (326 MPH) @ 18000 ft
- Max Fuel = 1007 lb
- Max Cabin Payload = 1000 lb
- Payload at Max Fuel = 865 lb
- Max Cruise @ 22000ft (75% power) = 264 Knots (304 MPH) @ 1500 Nautical Miles Range*
- Economy Cruise @ 24000ft (50% power) = 210 Knots (242 MPH) @ 2100 Nautical Miles Range*
- Cabin Pressurized to 7000 ft at 22,000 ft altitude
- Aspect Ratio = 13.2
- Electric Retract gear
- Full-Span Aileron Reflex
- Five-Place Seating/1 bed
- Boom Baggage

*Range includes Takeoff, climb and 45 min reserve

Figure 1.2 - Rutan Boomerang specifications.

1.4 Open Vehicle Sketch Pad (VSP)

Open Vehicle Sketch Pad (OpenVSP) is an open-source software platform developed by NASA to support the design and analysis of three-dimensional (3D) parametric models of aircraft. It is particularly well-suited for conceptual design tasks, allowing for the rapid development and assessment of both traditional and unconventional aircraft configurations. OpenVSP was released as open source in 2012 under the NASA Open-Source Agreement and continues to evolve with contributions from NASA, the Air Force Research Laboratory (AFRL), and the broader aerospace community.

1.4.1 Key Features

OpenVSP offers a versatile set of tools for aircraft design and analysis, catering to conceptual and early-stage development:

- **Parametric Geometry Modeling**: Users can create detailed 3D models using predefined shapes like wings, fuselages, and propellers, as well as advanced geometries such as ducts and bodies of revolution. The user-friendly interface combines a workspace for visualization and a geometry browser for managing and modifying components, streamlining the modeling process.

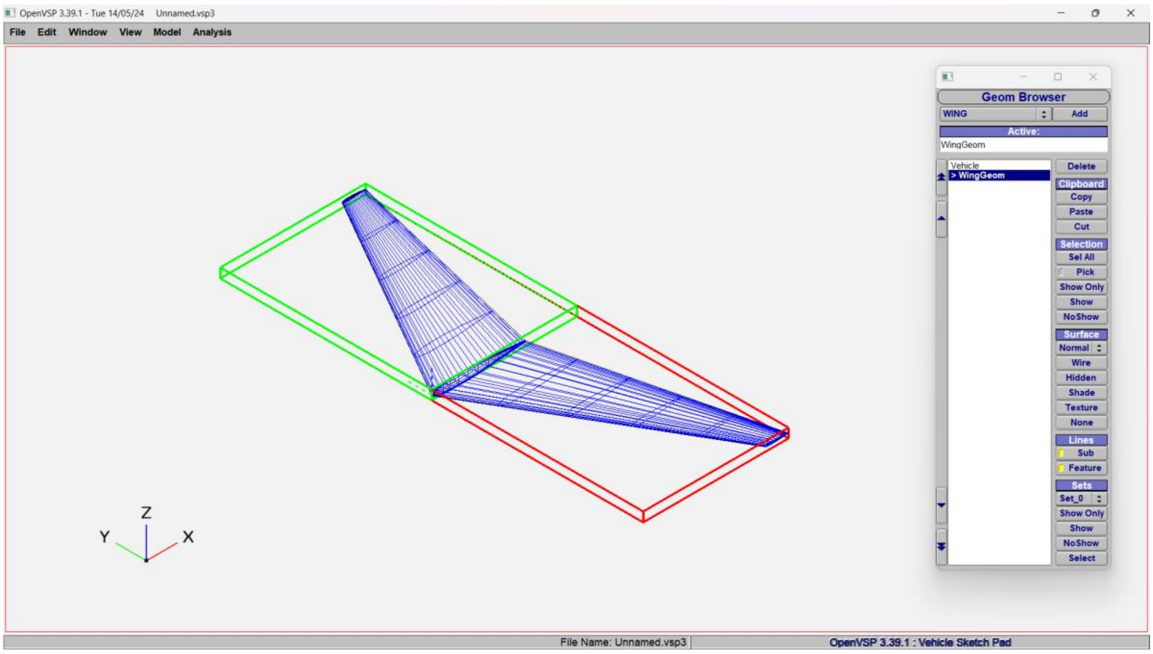

Figure 1.3 - OpenVSP User Interface

- **Aerodynamic Analysis**: Tools like VSPAERO provide aerodynamic evaluations using vortex lattice and panel methods, while additional features estimate wave and parasite drag for performance assessments.
- **Structural Analysis**: OpenVSP supports finite element analysis (FEA) by generating meshes and designing internal structures such as ribs and spars, aiding in structural integrity evaluations.

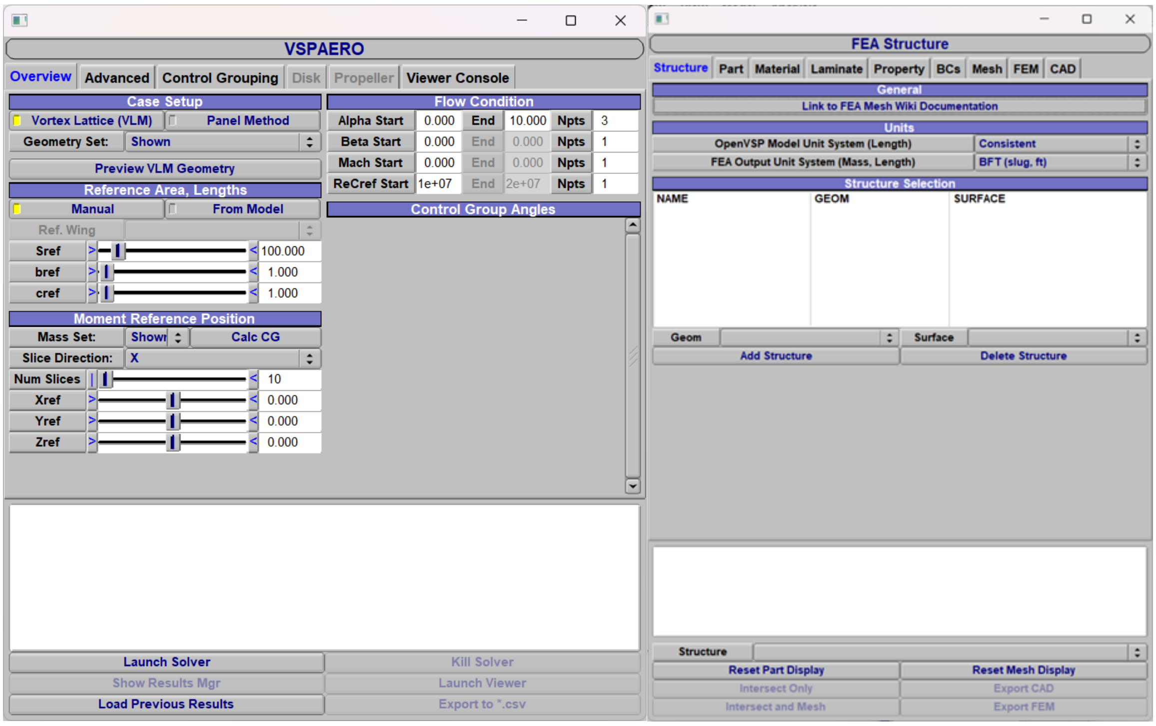

Figure 1.4 - VSPAERO & FEA Structure tabs

- **Geometry Processing and Simplification**: The CompGeom tool handles mesh generation, intersections, and trimming, while simplified geometry representations can be created for specific analyses.
- **File Compatibility and Integration**: The software supports importing and exporting formats like STL, STEP, and IGES, ensuring compatibility with CFD and FEA tools. Scripting via Python, MATLAB, and AngelScript allows for workflow automation and customization.

1.4.2 Applications

OpenVSP is widely used in conceptual aircraft design, facilitating efficient model iteration and testing. Its export capabilities enable detailed aerodynamic and structural analysis in specialized software. It also serves as a teaching and research tool for aerospace design.

1.5 Vortex Lattice Method (VLM)

The **Vortex Lattice Method (VLM)** is a numerical approach in aerodynamics that predicts aerodynamic forces and moments on wings and other lifting surfaces. It is widely used during the conceptual stages of aircraft design due to its efficiency and ability to model various geometries within certain assumptions.

1.5.1 Theoretical Foundations

The VLM is based on the following principal aerodynamic theories:

- **Potential Flow Theory**: the fluid is assumed to be incompressible, inviscid, and irrotational. These assumptions simplify the governing equations of fluid motion, allowing the use of Laplace's equation for the velocity potential, expressed as:

$$\nabla^2 \phi = 0 \tag{1.1}$$

  where ϕ represents the velocity potential.

- **Kutta-Joukowski Theorem**: the lift per unit span (l) generated by a vortex filament is proportional to the circulation (Γ) around it and the free-stream velocity (V_∞):

$$l = \rho V_\infty \Gamma \tag{1.2}$$

  where ρ is the air density.

- **Helmholtz's Vortex Theorems**: the strength of a vortex filament remains constant along its length, and vortices either form closed loops or terminate at physical boundaries such as surfaces.

1.5.2 Assumptions

The Vortex Lattice Method relies on the following assumptions:

- **Flow Properties**: The flow is treated as incompressible, inviscid, and irrotational. Nonetheless, small-disturbance subsonic compressible flow can be accommodated by applying the general 3D Prandtl-Glauert transformation.
- **Lifting Surface Characteristics**: The lifting surfaces are assumed to be thin, and the effects of surface thickness on aerodynamic forces are disregarded.

- **Small Angle Approximations**: Both the angle of attack and sideslip are considered small, allowing for the use of linear approximations in the analysis.

1.5.3 Numerical Representation of the Wing

In the numerical representation of the wing, thickness is disregarded: in fact, it is simplified to a surface that has the same camber of the selected airfoil, while fuselages are represented by two intersecting mean surfaces forming a cross. Instead of the classical VLM approach, which consists of dividing the mean surface of wing into a grid of panels each containing a bound vortex line that models the circulation along the surface, VSPAERO solves the lifting surface problem by vortex ring elements. The main advantage of this element is in the simple programming effort that it requires, although its computational efficiency can be further improved.

The following key elements define the numerical approach:

- **Bound Vortices**: Located at the quarter-chord line of each panel to represent the lift.
- **Control Points**: Placed at the three-quarter chord line of each panel to enforce boundary conditions.

The unknown circulation strengths (Γ_i) are solved using boundary conditions and the Biot-Savart law.

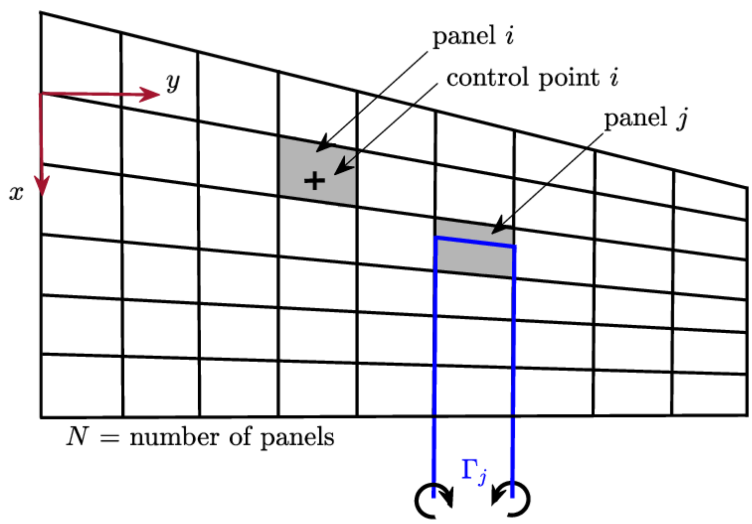

Figure 1.5 - Panelling and horseshoe vortex placement for a right wing.

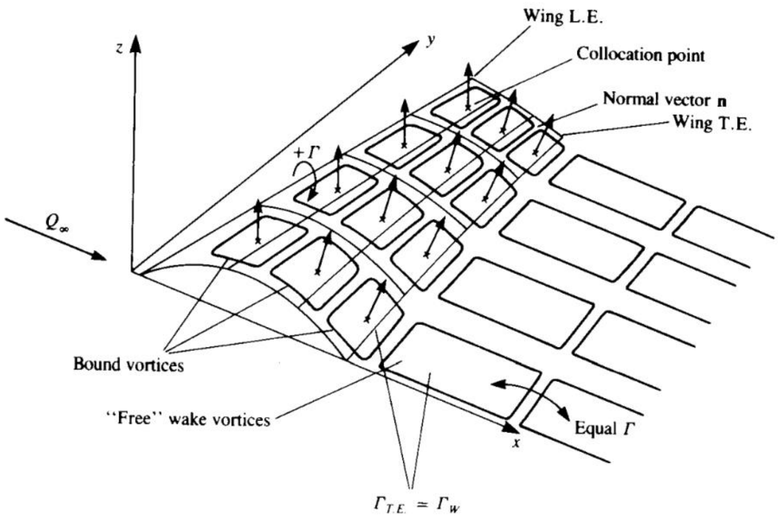

Figure 1.6 - Vortex ring model for a thin lifting surface

1.5.4 Velocity Induction and Biot-Savart Law

The Biot-Savart law determines the velocity induced by a vortex filament at a given point:

$$\mathbf{v} = \frac{\Gamma}{4\pi}\int \frac{\mathbf{r_1}\times\mathbf{r_2}}{|\mathbf{r_1}\times\mathbf{r_2}|^3}\, d\boldsymbol{s} \tag{1.3}$$

Here:

- Γ represents the vortex strength.
- $\mathbf{r_1}$ and $\mathbf{r_2}$ are vectors connecting the vortex element to the point of interest.
- $d\boldsymbol{s}$ denotes an infinitesimal segment of the vortex filament.

This relationship quantifies the induced velocity field, which forms the basis for satisfying the flow conditions at control points.

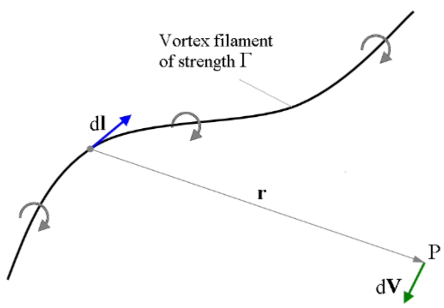

Figure 1.7 - Line vortex

1.5.5 Boundary Condition: No-Penetration

The boundary condition ensures that fluid flow remains tangent to the surface of the wing, expressed mathematically as:

$$\boldsymbol{V} \cdot \boldsymbol{n} = 0 \tag{1.4}$$

Here:

- V is the total velocity at the control point, combining free-stream velocity (V_∞) and induced velocity (v).
- n is the normal vector at the control point.

Substituting the induced velocity components into this equation for all control points results in a system of linear equations that relate the vortex strengths to the flow field.

1.5.6 Solution of Linear Equations

The governing equations from the no-penetration condition can be expressed in matrix form:

$$[A]\{\Gamma\} = \{-V_\infty \cdot n\} \tag{1.5}$$

where:

- $[A]$ is the influence coefficient matrix, representing the effect of all vortex filaments on each control point.
- $\{\Gamma\}$ is the vector of unknown vortex strengths.
- $\{-V_\infty \cdot n\}$ represents the free-stream contribution.

Solving this system yields the circulation distribution (Γ) for the wing panels.

1.5.7 Lift Calculation

Once the circulation distribution is determined, the lift force is calculated using the Kutta-Joukowski theorem:

$$L = \rho V_\infty \sum_{i=1}^{N} \Gamma_i \Delta y \tag{1.6}$$

where Γi is the vortex strength for panel i and Δy represents the spanwise width of the panel.

1.5.8 Induced Drag

Induced drag arises from the downwash effects caused by trailing vortices. The induced drag can be calculated as:

$$D_i = \rho \sum_{i=1}^{N} \Gamma_i w_i \Delta y \tag{1.7}$$

Where w_i is the downwash velocity at the control point, which is computed from the trailing vortices using the Biot-Savart law.

1.5.9 Wake Modeling

In the VLM, trailing vortices extend downstream into the wake. While the simplest models assume a planar wake, more advanced methods allow the wake to deform naturally under flow conditions. The induced velocity contribution from the wake is given by:

$$\mathrm{w_w} = \frac{\Gamma}{4\pi} \int_{\mathrm{wake}} \frac{\mathbf{r_1} \times \mathbf{r_2}}{|\mathbf{r_1} \times \mathbf{r_2}|^3}\, d\mathbf{s} \tag{1.8}$$

Accurate wake modeling is essential for improving the accuracy of drag predictions.

1.5.10 Simplifications and Practical Application

- **Panel Influence Calculation**: The contribution of each vortex filament to the velocity field is precomputed, reducing the computational effort during the solution phase.
- **Numerical Solution**: Efficient solvers are used to solve the system of equations, making VLM computationally inexpensive compared to high-fidelity Computational Fluid Dynamics (CFD) simulations.

1.5.11 Limitations

The Vortex Lattice Method (VLM) inherently focuses on lifting surfaces (e.g., wings, horizontal and vertical tails) and treats the flow around non-lifting components like fuselages, pylons, or nacelles as secondary. This limitation arises because VLM does not account for the aerodynamic effects of these components unless explicitly included as lifting surfaces, which may not accurately capture their actual role in the flow field. Lastly, the Vortex Lattice Method (VLM) neglects parasite drag, including skin friction, form, and interference drag, leading to incomplete and potentially inaccurate drag predictions.

2. Geometric Modelling

2.1 Rutan Boomerang general aspects

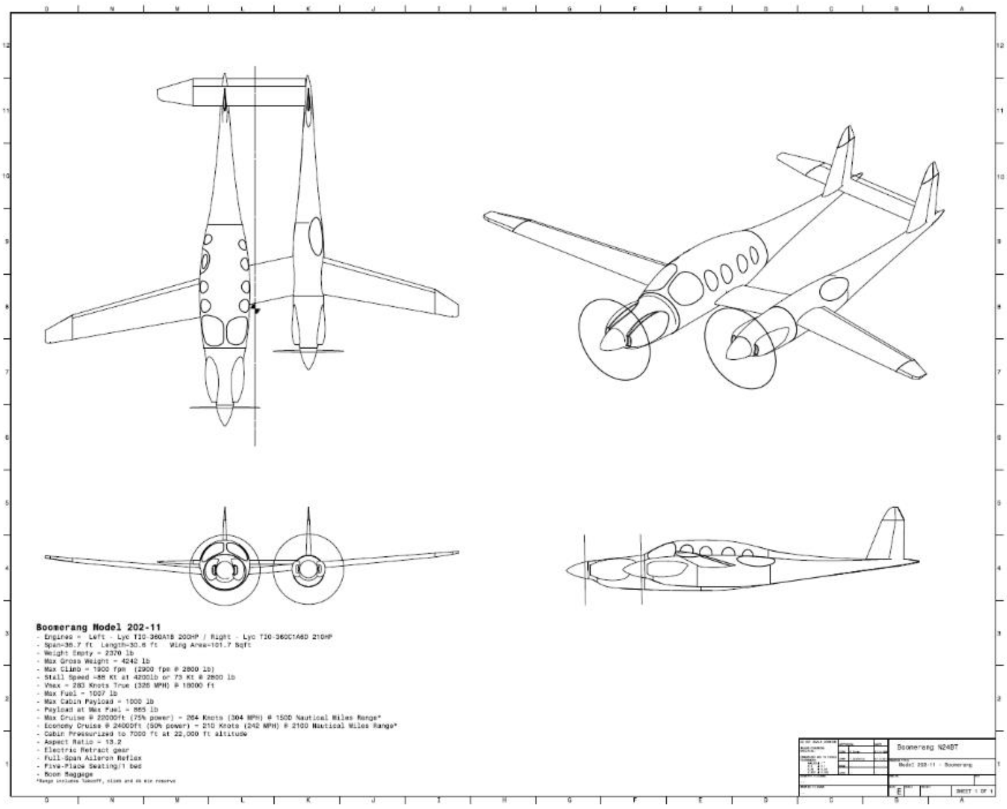

Figure 2.1 - Rutan Boomerang general views drawing

From the drawing specifications, only the span (36.7 ft) length (36.0 ft) and wing area (101.7 Sq ft) are available. Starting from the exact given value, the right fuselage model length has been set. Other measurements have been estimated through the Adobe Measurements Tool, as they will be inserted as starting values for the various default geometries from Open VSP. It is possible to set different backgrounds corresponding to the different views. This is crucial for the user to adjust the measurements of the model to have perfect alignment of the contours. In this work, perfect alignment cannot be obtained due to a misalignment error present in the drawing, more specifically, the distance from left fuselage to the right in the top and front are not equal. The latter distance has been chosen for the model. For meshing refinement, the methodology aligns with best practices recommended by the OpenVSP community and the OpenVSP Google Group.

2.2 Rutan Boomerang components modeling and meshing

2.2.1 Wing

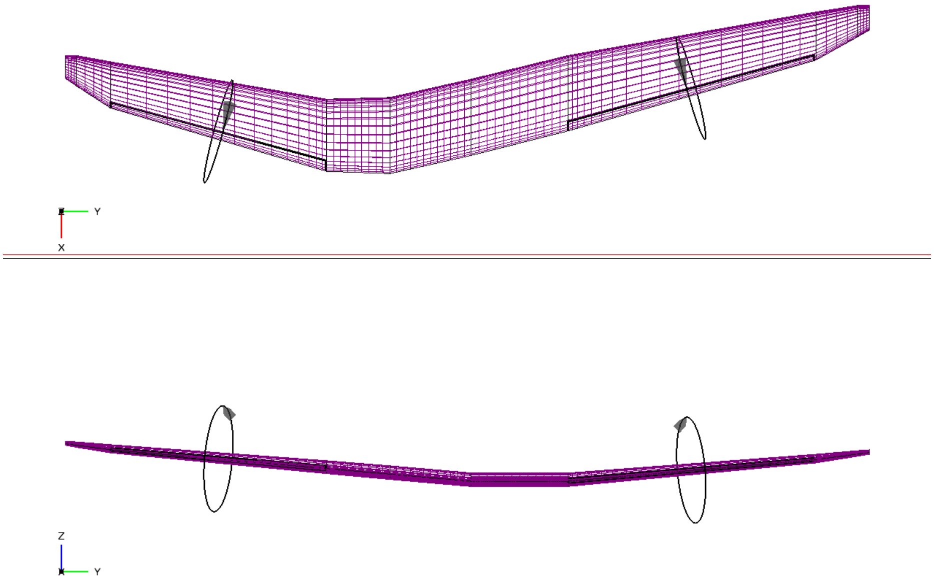

Figure 2.2 - Wing model top and rear views

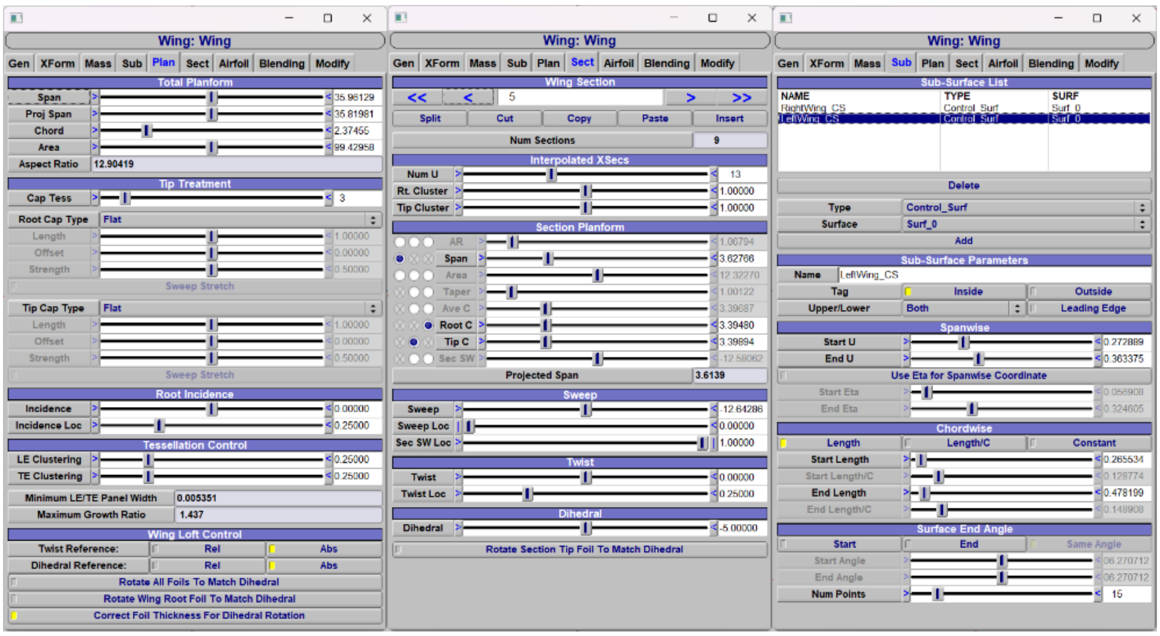

Figure 2.3 - Wing model parameters

The asymmetrical wing is represented through a model comprising eight distinct parts to account for its geometrical complexity. The airfoil utilized is a NACA 2218 profile, and the flaperons exhibit a positive deflection when rotated downward (counterclockwise about the *y*-axis in the OpenVSP reference frame). When functioning as ailerons, deflected in an antisymmetric manner, a positive deflection corresponds to a downward deflection of the right aileron, resulting in a negative rolling moment (clockwise rotation about the *x*-axis in the OpenVSP reference frame). Additional parameters are detailed in Figure 2.3.

2.2.2 Fuselages

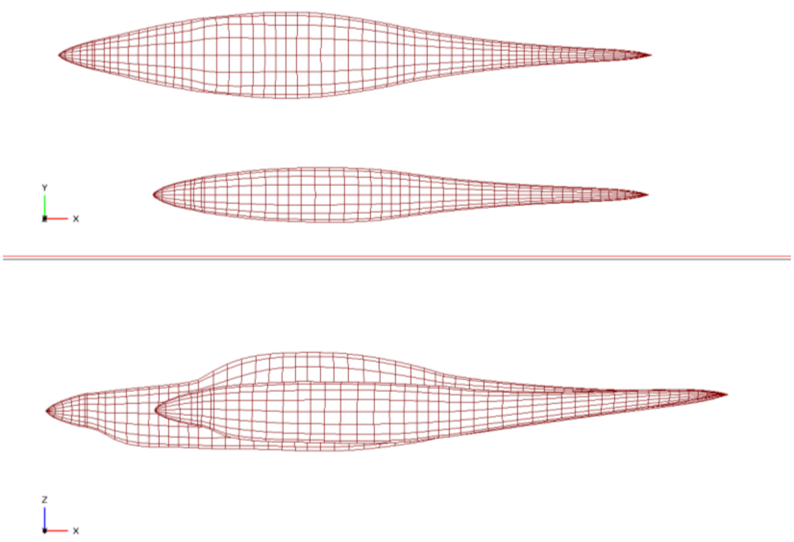

Figure 2.4 - Fuselages model top and left view

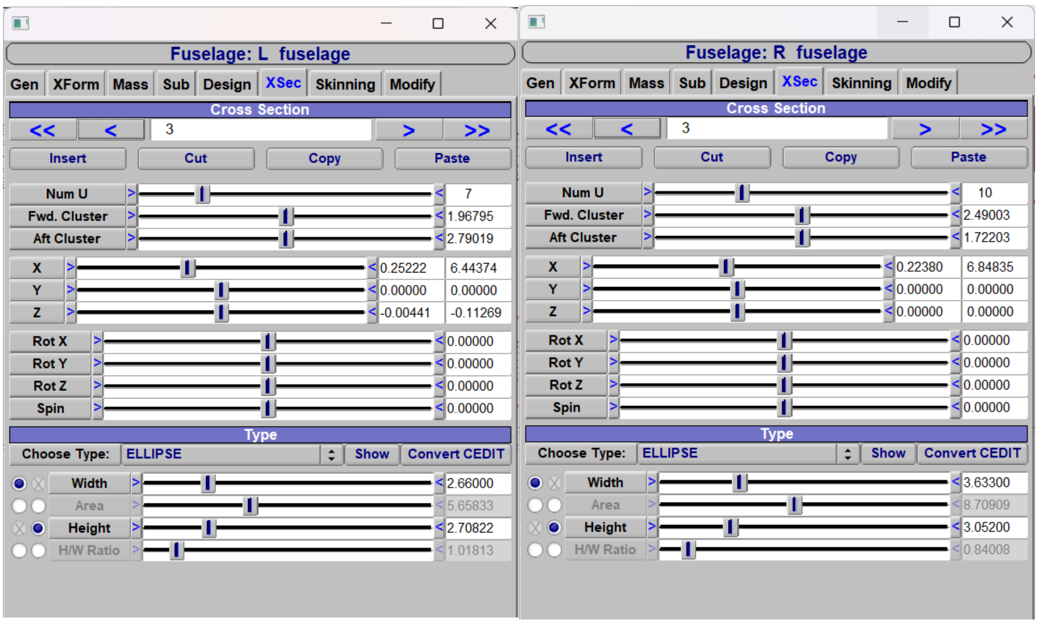

Figure 2.5 - Fuselages model section 3 parameters

2.2.3 Horizontal tail

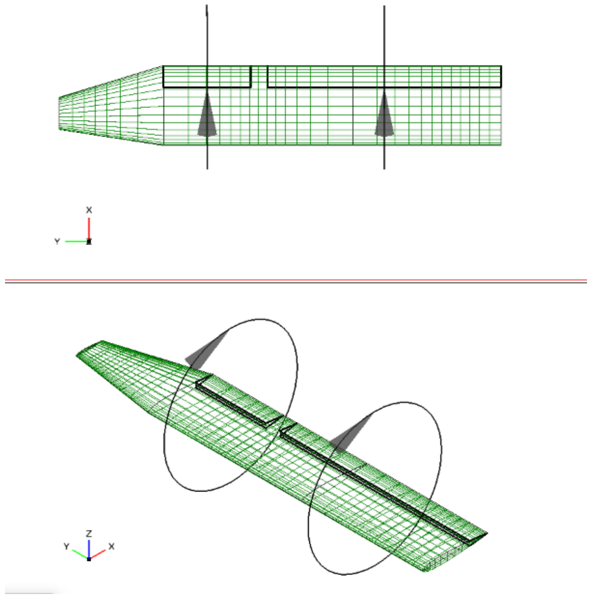

Figure 2.6 - Horizontal tail model top and iso left view

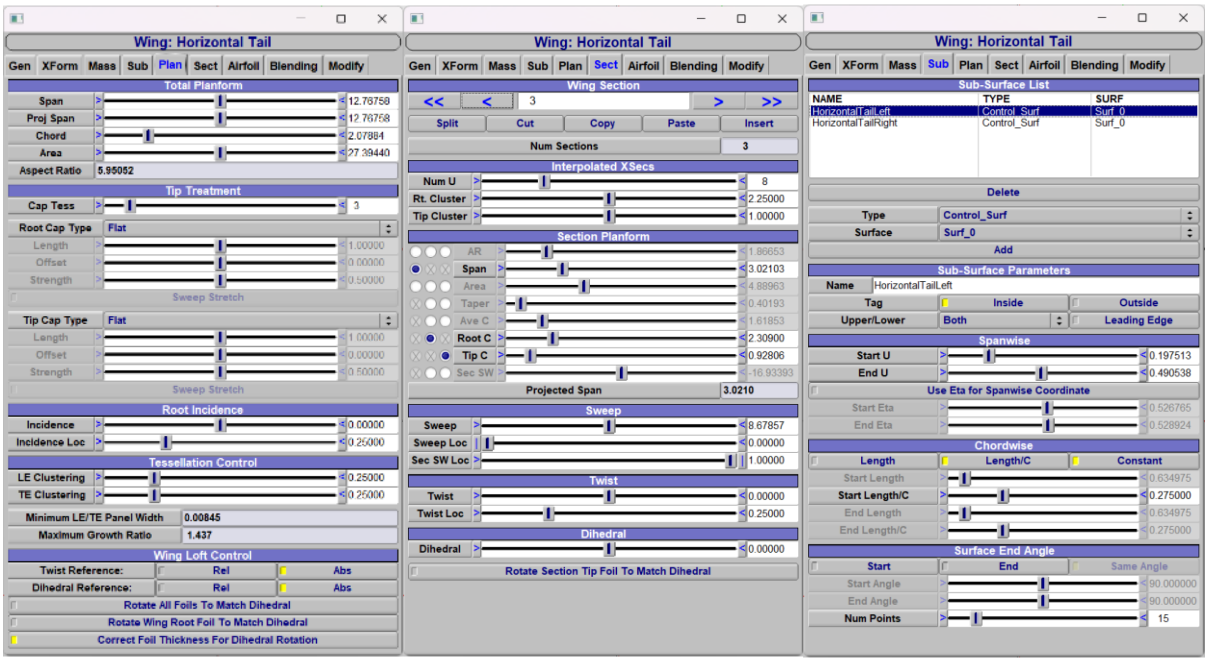

Figure 2.7 - Horizontal tail model parameters

The elevators exhibit a positive deflection when rotated downward (counterclockwise about the y-axis in the OpenVSP reference frame). This results in a negative pitching moment (clockwise rotation about the y-axis in the OpenVSP reference frame). Additional parameters are detailed in Figure 2.7.

2.2.4 Vertical tail

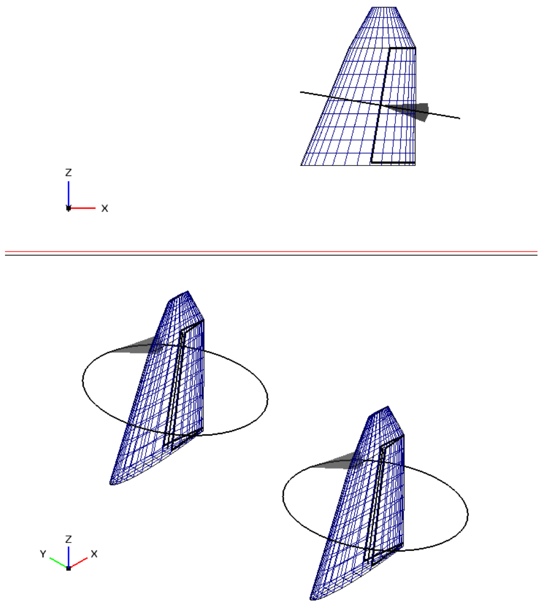

Figure 2.8 - Vertical tail model top and left views

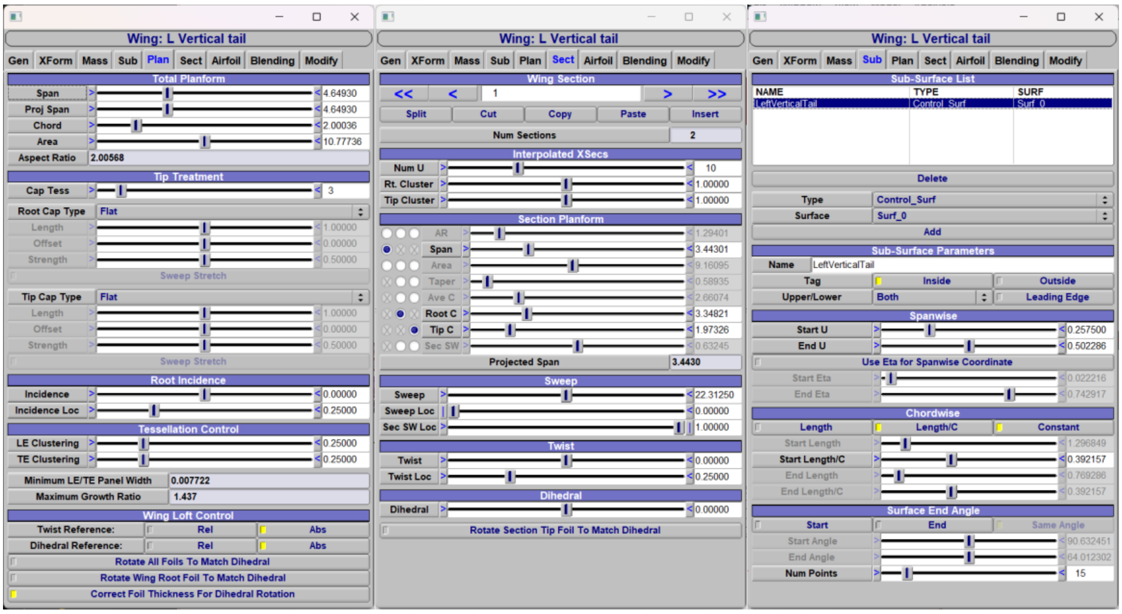

Figure 2.9 - Vertical tail model parameters

The rudders exhibit a positive deflection when rotated to the right (counterclockwise about the z-axis in the OpenVSP reference frame). This results in a negative yawing moment (clockwise rotation about the z-axis in the OpenVSP reference frame). Additional parameters are detailed in Figure 2.9.

2.2.5 Other components

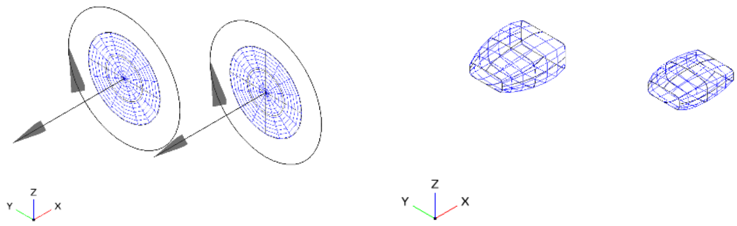

Figure 2.10 - (Left) Propeller modelled as an actuator disk. (Right) Air ducts

The propellers, modeled as actuator disks, have a diameter of 6.1 ft. The air ducts have been modeled with OpenVSP's stack component. Propellers will be considered exclusively during propulsive effects analysis, meanwhile airducts will be completely neglected.

2.3 Aircraft model views

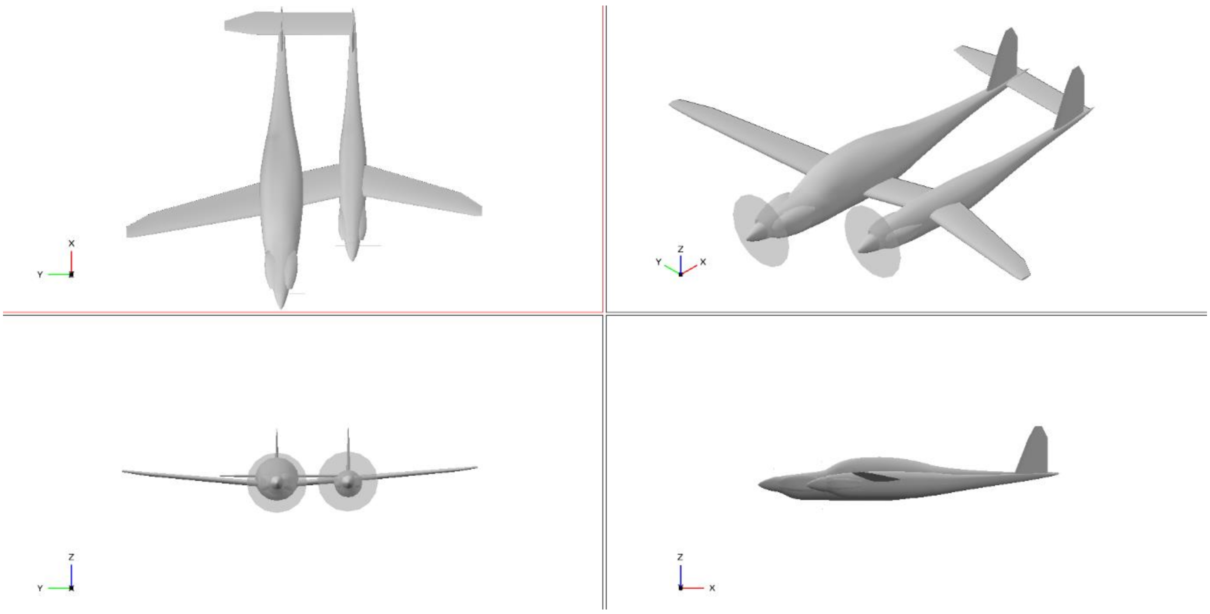

Figure 2.11 - Rutan Boomerang's model general views

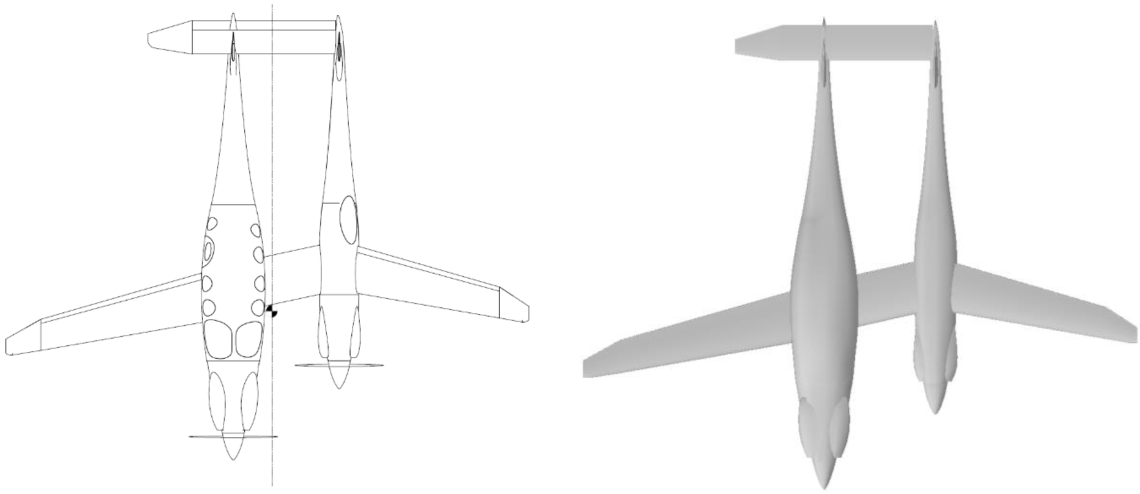

Figure 2.12 - Top view side by side comparison

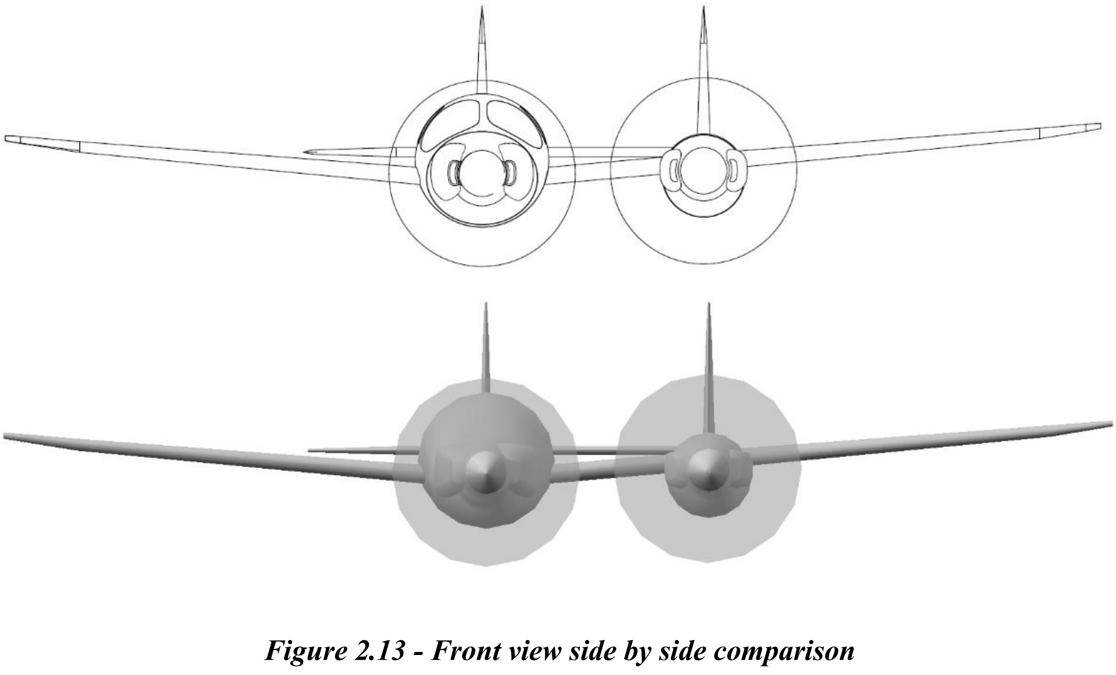

Figure 2.13 - Front view side by side comparison

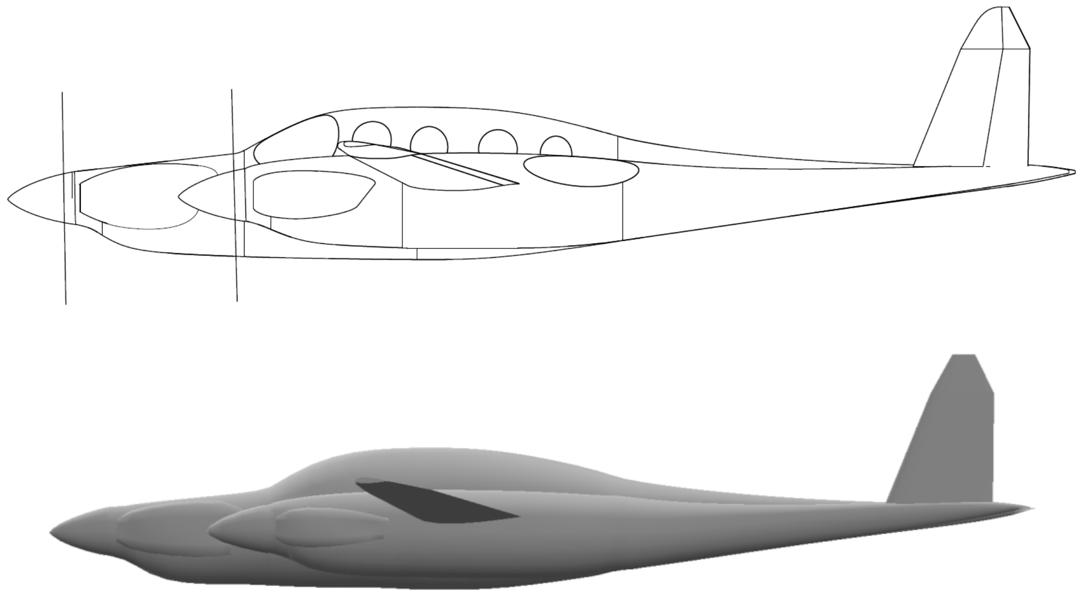

Figure 2.14 - Left view side by side comparison

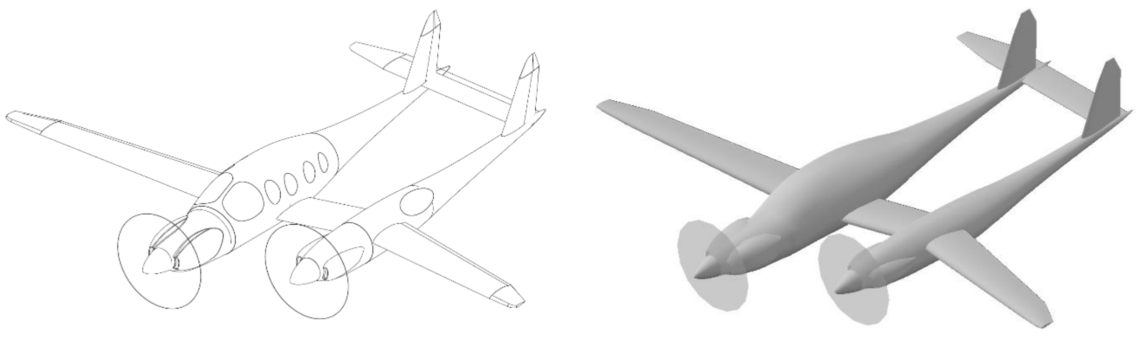

Figure 2.15 - Left iso view side by side comparison

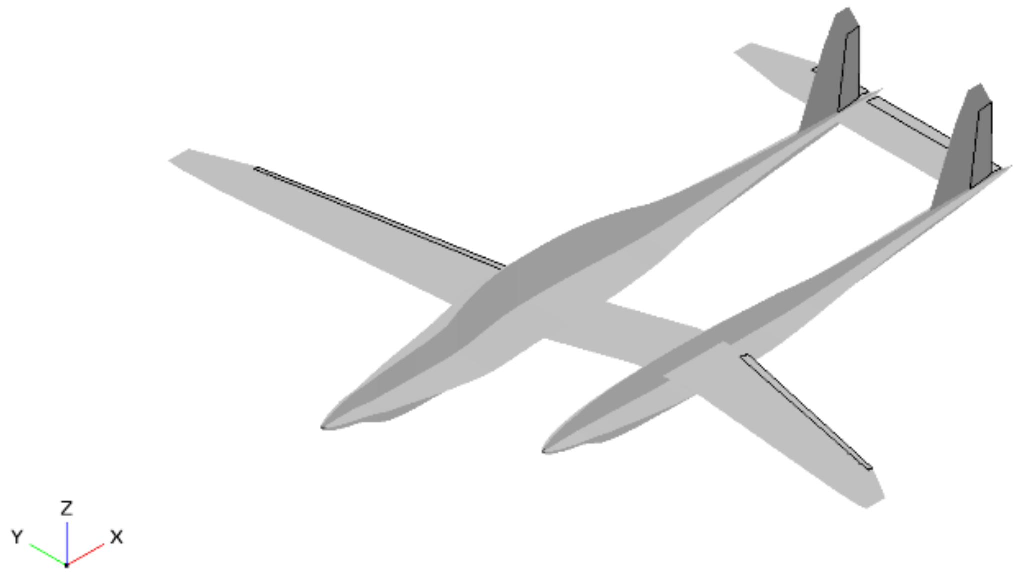

Figure 2.16 - Left iso view of the mean surface

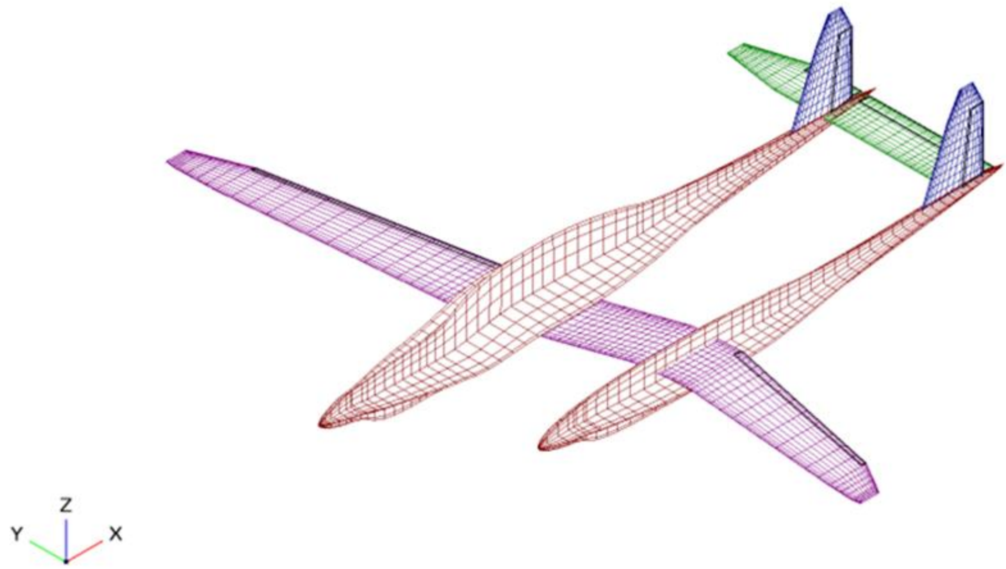

Figure 2.17 - Left iso view of the meshed mean surface

3. Longitudinal aerodynamic analysis

3.1 Analysis setup

3.1.1 Sets

The following sets have been defined for the longitudinal aerodynamic analysis, to see how the coefficients vary from the isolated wing to the complete aircraft. As said before, propellers and airducts will be neglected during the analysis. Therefore, the Wing-Body-Tail (WBT) set will be referred to as the whole aircraft from now on.

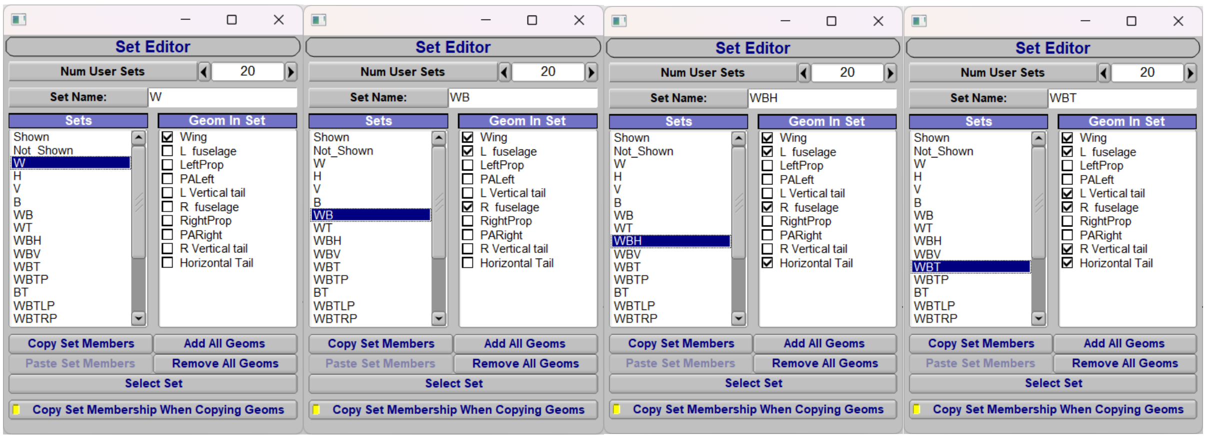

Figure 3.1 - Set editor tabs

3.1.2 Center of gravity

The center of gravity is chosen as moment reference pole. Its position has been defined from its position from the aircraft drawing. The coordinates are relative to the Open VSP reference frame, which origin is coincident to the right fuselage's nose tip.

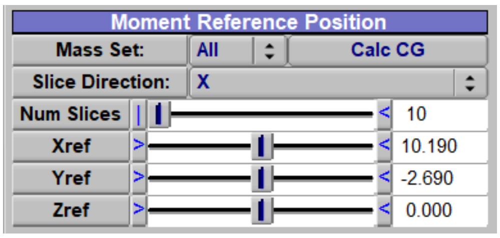

Figure 3.2 - Moment reference position tab

3.1.3 Flow condition

According to the aircraft's specifications, an economy cruise at $24000\,ft$, 50% power, $210knots(242mph)$has been chosen as the flight condition for this analysis. This means that the Mach number is equal to $0{,}347$ and the Reynolds number to $2{,}74496e+06$. This condition will be considered in both longitudinal and lateral-directional analysis.

3.1.4 Data processing

The csv (Comma Separated Values) files generated by the analysis have been processed through a MATLAB code that automatically generates Microsoft Excel Sheets containing the tables that are found below and the aerodynamic derivatives of interest, estimated through first order polynomial interpolation.

3.2 Clean configuration

For this analysis, control surfaces are set to zero deflection. The angle of attack (α) interval considered is from $\alpha = 0°$ to $12°$ with a step of $2°$, within the linearity range.

3.2.1 Lifting surfaces load distribution

The following diagrams are the results of the analysis conducted on the WBT set.

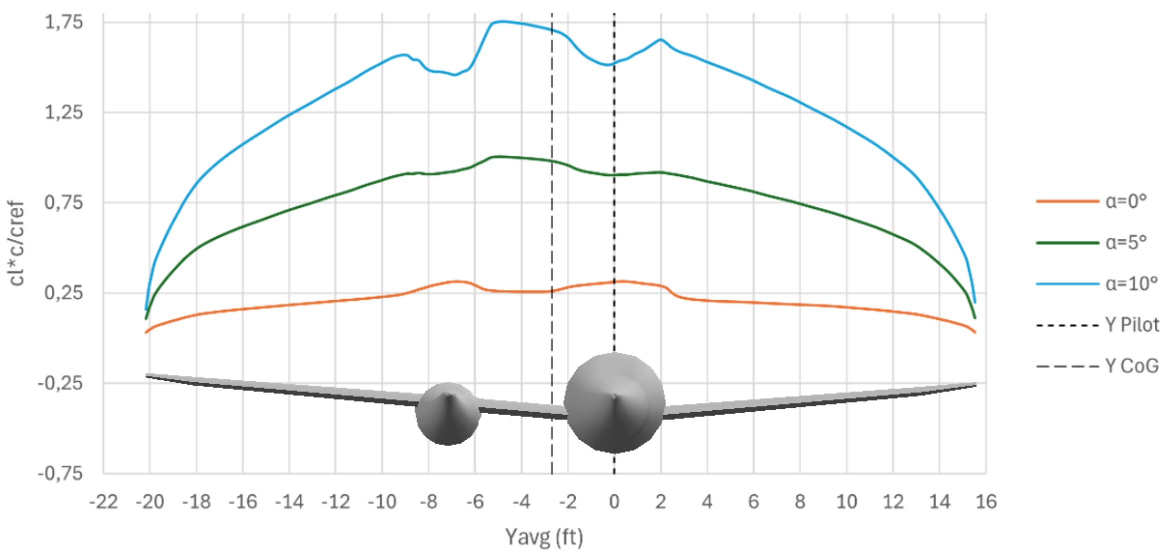

Figure 3.3 - Wing load distribution diagram varying with α°

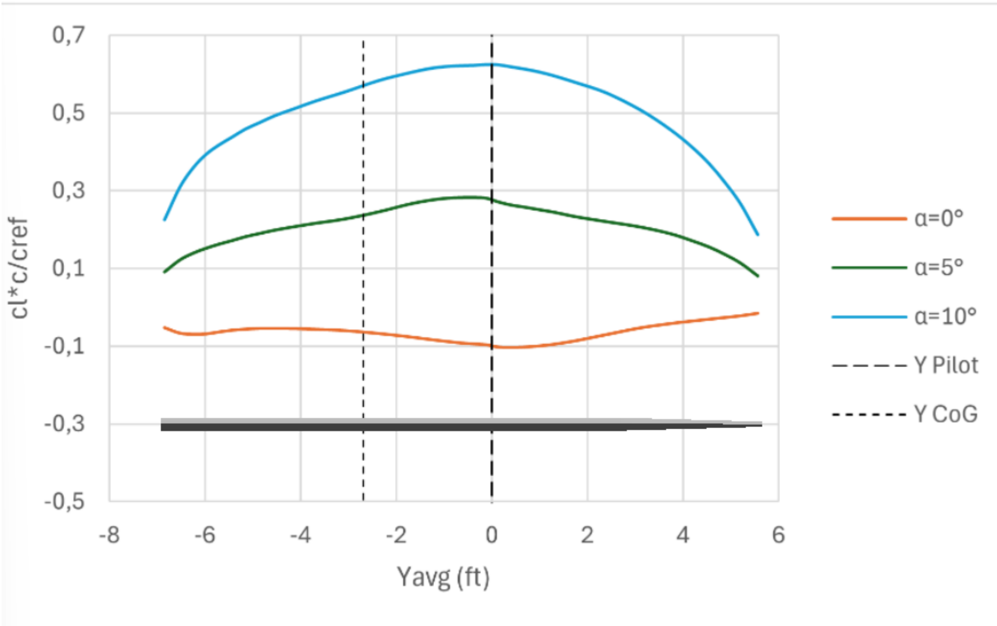

Figure 3.4 - Horizontal tail load distribution diagram varying with α°

Due to the asymmetric shape of the airplane, it is reasonable to expect that the load is also asymmetric. Furthermore, the influence of the fuselages on the loading is notable. Pressure distribution and trailing wakes can be seen by opening VSPAERO's viewer.

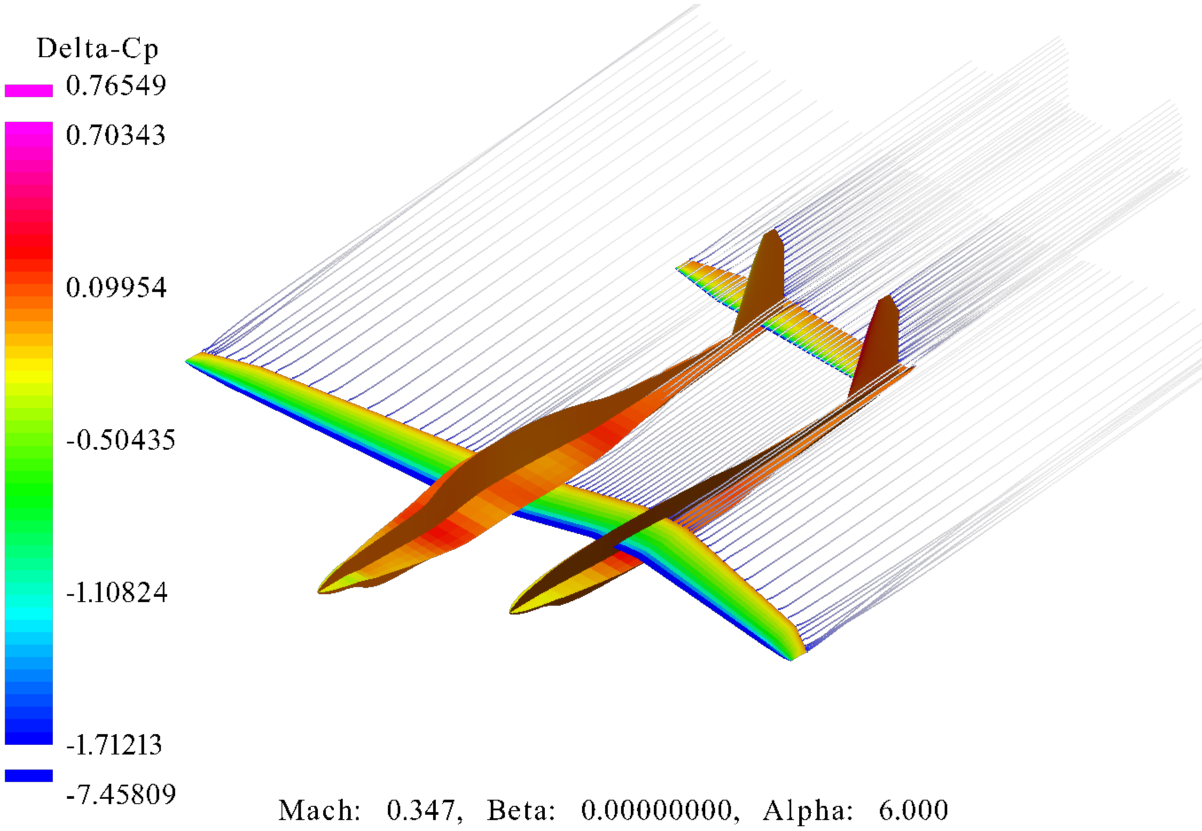

Figure 3.5 - Pressure distribution and trailing wakes from VSPAERO Viewer for $\alpha =$ 6°

3.2.2 Lift Coefficient

For each defined set, the analysis yields the following values for the *lift coefficient* (C_L).

$\alpha°$	W	WB	WBH	WBT
0	0,168	0,176	0,157	0,156
2	0,355	0,363	0,376	0,376
4	0,544	0,550	0,596	0,596
6	0,731	0,737	0,817	0,818
8	0,919	0,923	1,039	1,039
10	1,106	1,109	1,260	1,262
12	1,292	1,294	1,484	1,485

Table 3.1 - C_L values vs $\alpha°$

By plotting the given values of C_L w.r.t. α, we obtain:

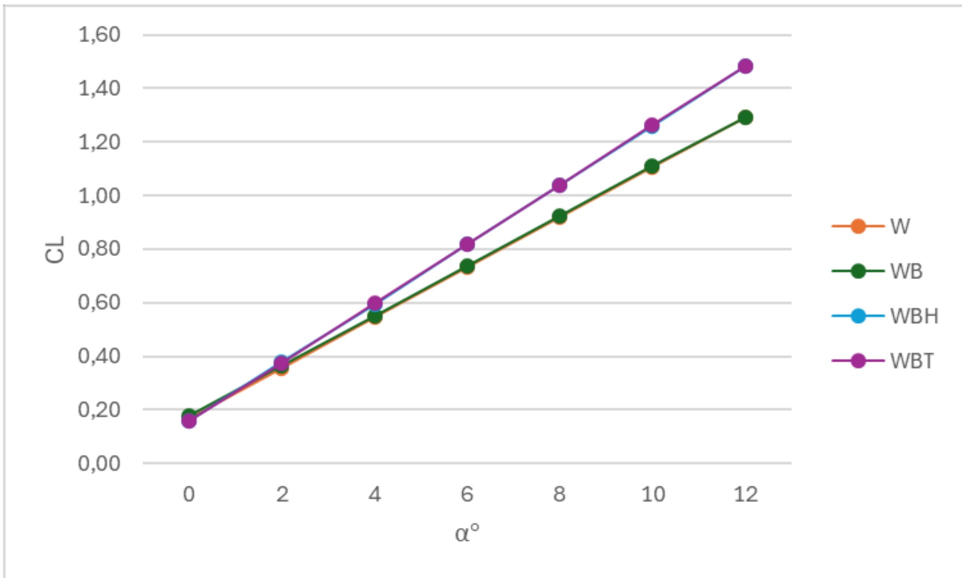

Figure 3.6 - C_L vs $\alpha°$

While the values of C_L do not differ by adding the fuselages to the wing, a variation is notable when the tail is also considered.

The total aircraft's lift curve slope is:

$$C_{L\alpha} = 0{,}1107\ deg^{-1} \tag{3.1}$$

3.2.3 Drag coefficient

For each defined set, the analysis yields the following values for the *drag coefficient* (C_D).

$\alpha°$	W	WB	WBH	WBT
0	0,0091	0,0082	0,0104	0,0122
2	0,0122	0,0116	0,0142	0,0161
4	0,0175	0,0177	0,0216	0,0235
6	0,0248	0,0264	0,0328	0,0348
8	0,0344	0,0379	0,0476	0,0497
10	0,0460	0,0519	0,0659	0,0682
12	0,0596	0,0687	0,0881	0,0904

Table 3.2 - C_D values vs $\alpha°$

By plotting the given values of C_D w.r.t. α, we obtain:

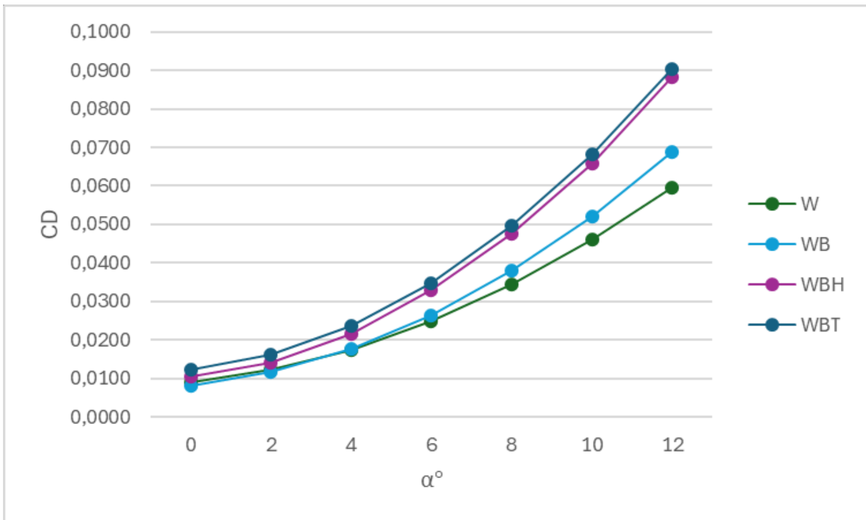

Figure 3.7 - C_D vs $\alpha°$

Drag increases with α due to the increase of induced drag. Note that VSPAERO includes an estimate of parasite drag C_{D0} in the calculation of the zero lift drag coefficient, but it is best practice to utilize the *Parasite Drag* tool, which provides much more advanced options and capabilities. Parasite drag is a combination of form, friction, and interference drag that is evident in any body moving through a fluid. For the $friction\ coefficient\ C_f$, different equations are available, so the Blasius equation for laminar flow and the Blasius power law for turbulent flow have been selected. Regarding Form Factor FF, the DATCOM method has been chosen.

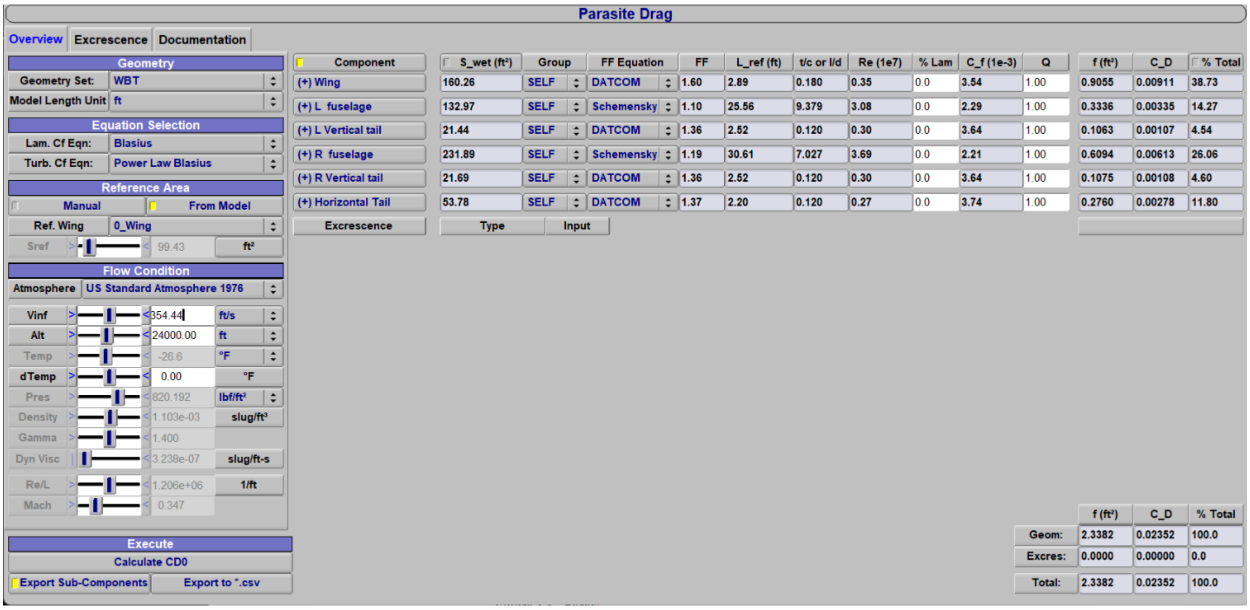

Figure 3.8 - Parasite Drag graphical user interface for WBT set

For each defined set, the computation yields the following values for the zero lift drag coefficient (C_{D0}).

	W	WB	WBH	WBT
C_{D0}	0,0118	0,0187	0,0214	0,0235

Table 3.3 - C_{D0} values

Given C_{Di} , that is the lift induced drag coefficient, calculated by the VSPAERO tool, and knowing that:

$$C_D = C_{D0} + C_{Di} \tag{3.2}$$

a better estimation of C_D can be obtained, as presented below.

$\alpha°$	W	WB	WBH	WBT
0	0,0125	0,0185	0,0211	0,0232
2	0,0149	0,0213	0,0243	0,0263
4	0,0191	0,0263	0,0306	0,0327
6	0,0251	0,0336	0,0402	0,0423
8	0,0328	0,0431	0,0530	0,0552
10	0,0422	0,0550	0,0689	0,0712
12	0,0532	0,0692	0,0882	0,0906

Table 3.4 - C_D enhanced values vs $\alpha°$

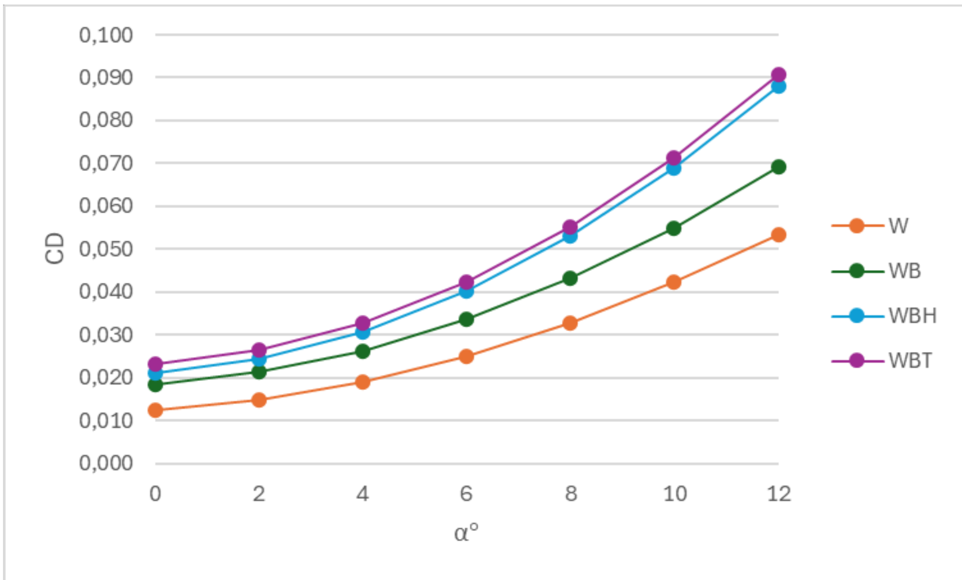

Figure 3.9 - C_D enhanced vs α°

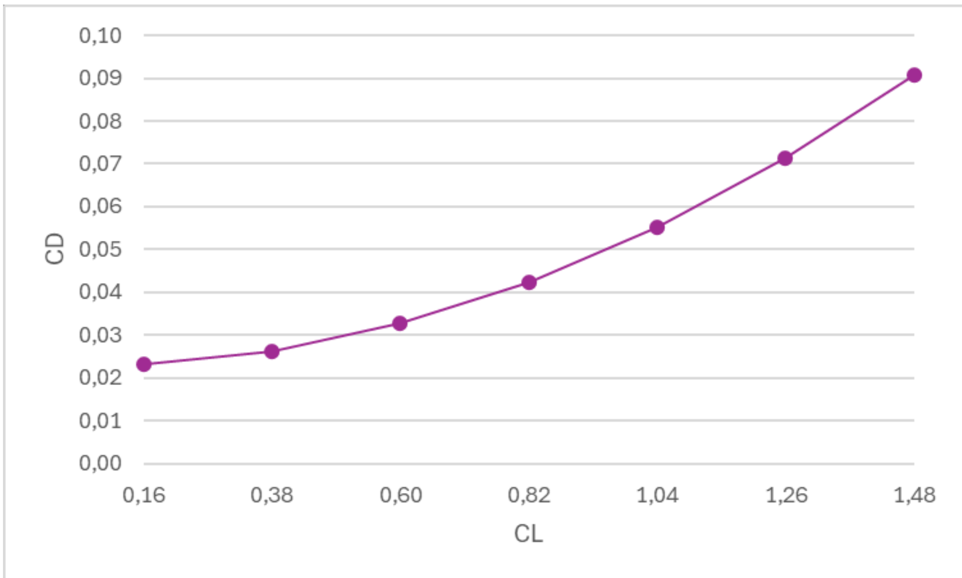

Figure 3.10 - Aircraft C_D vs C_L curve

3.2.4 Aerodynamic efficiency

For each defined set, the analysis yields the following values for the *lift/drag ratio (aerodynamic efficiency*, E), considering the C_D enhanced values computed above.

$\alpha°$	W	WB	WBH	WBT
0	13,44	9,52	7,45	6,74
2	23,83	17,09	15,51	14,27
4	28,44	20,95	19,49	18,26
6	29,18	21,96	20,35	19,33
8	28,05	21,39	19,62	18,84
10	26,22	20,16	18,30	17,71
12	24,26	18,71	16,83	16,38

Table 3.5 - E values vs α°

By plotting the given values of E w.r.t. α, we obtain:

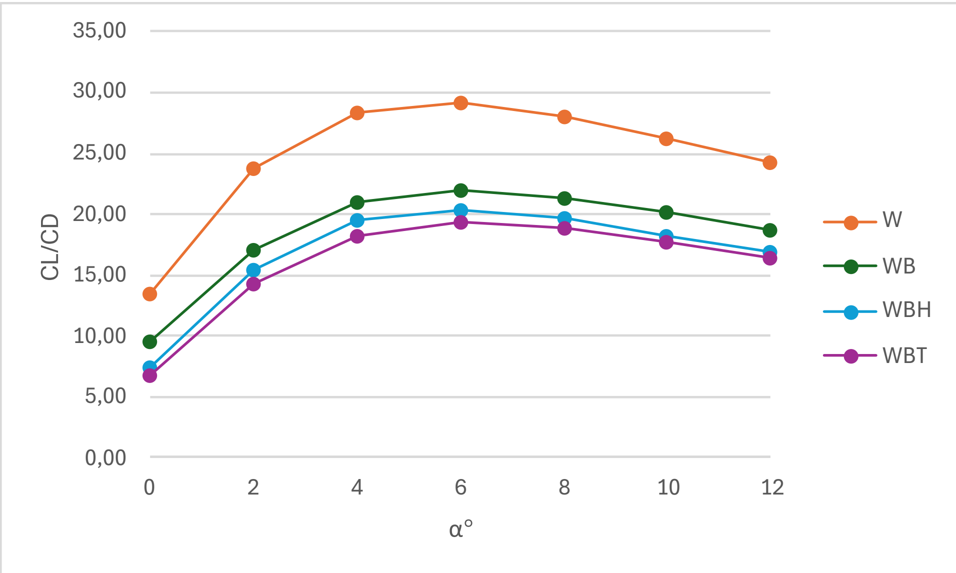

Figure 3.11 - E vs α°

E has its maximum around $\alpha = 6°$. As expected, it decreases the more components we consider, due to the higher drag.

3.2.5 Pitching moment coefficient

For each defined set, the analysis yields the following values for the *pitching moment coefficient* (C_{My}).

$\alpha°$	W	WB	WBH	WBT
0	-0,0765	-0,1563	-0,0149	-0,0056
2	-0,1102	-0,1265	-0,2226	-0,2214
4	-0,1463	-0,0976	-0,4386	-0,4491
6	-0,1849	-0,0700	-0,6701	-0,6859
8	-0,2257	-0,0468	-0,9109	-0,9299
10	-0,2690	-0,0252	-1,1596	-1,1809
12	-0,3143	-0,0065	-1,4243	-1,4424

Table 3.6 - C_{My} values vs $\alpha°$

By plotting the given values of C_{My} w.r.t. α, we obtain:

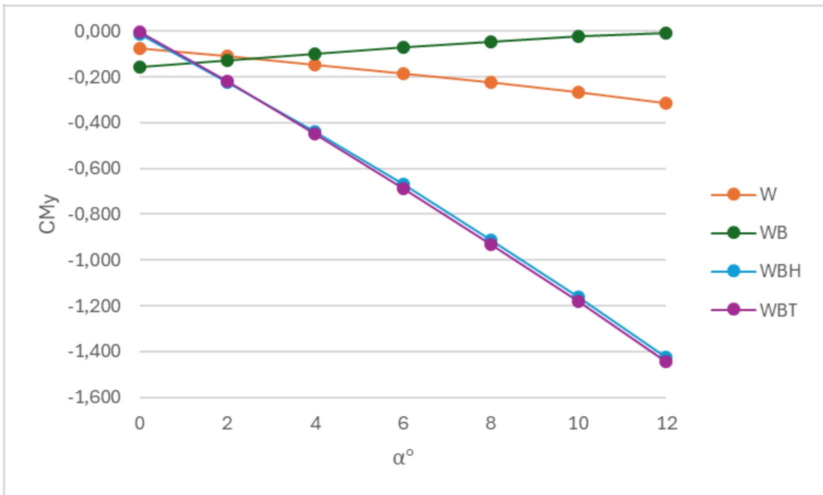

Figure 3.12 - C_{My} vs $\alpha°$

A positive slope of C_{My} indicates unstable behavior, as it suggests a nose-up pitching moment increases with angle of attack. This instability arises when fuselages are attached to the wing, but the addition of the tail counteracts this effect, restoring stability to the aircraft.

The aircraft's pitching moment curve slope is:

$$C_{My\alpha} = -0{,}1198\; deg^{-1} \tag{3.3}$$

This guarantees the aircraft's longitudinal stability. It can be shown that $C_{My\alpha}$ when C_L is zero is positive, meaning that the aircraft is also equilibrable.

3.3 Flaperon effects on longitudinal aerodynamics

For this analysis, control surfaces have a deflection set to zero, except for the flaperons acting as flaps. The flap deflection angle (δ_f) interval considered is from 0° to 20° with a step of 10°. The angle of attack α and sideslip angle β are fixed at 0°.

3.3.1 Lifting surfaces loading

The following diagrams are the results of the analysis conducted on the WBT set.

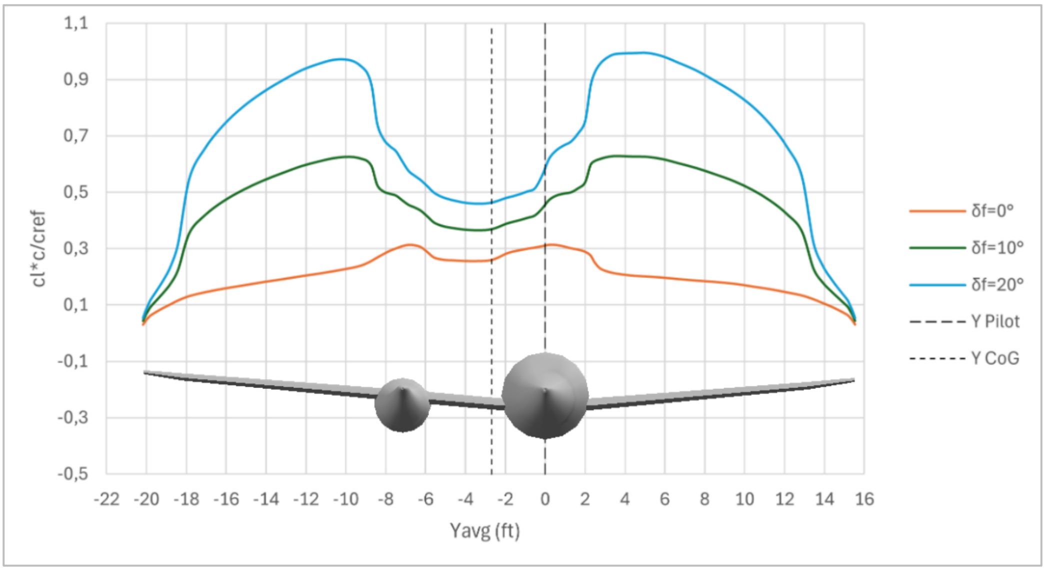

Figure 3.13 - Wing load distribution diagram varying with δ_f°

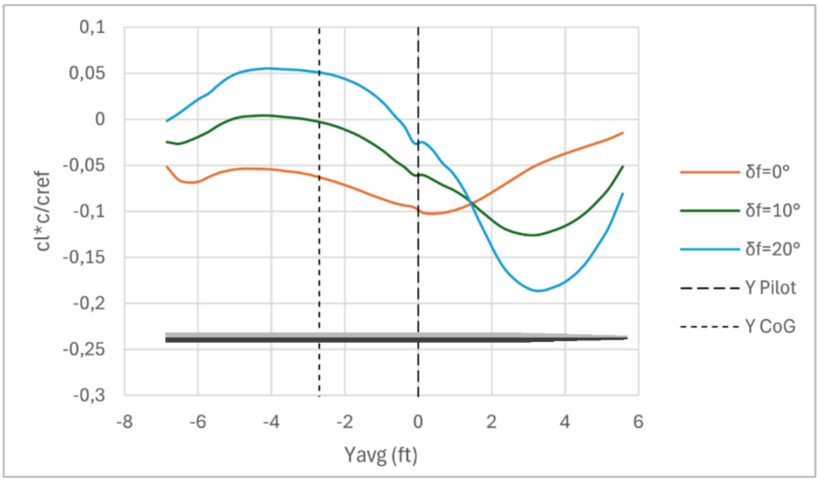

Figure 3.14 - Horizontal tail load distribution diagram varying with δ_f°

It is possible to note that C_l increases significantly along the span of the flaperons. A decrease of C_l on the right part of the horizontal tail is due to the decrease of its angle of attack caused by the wing wake.

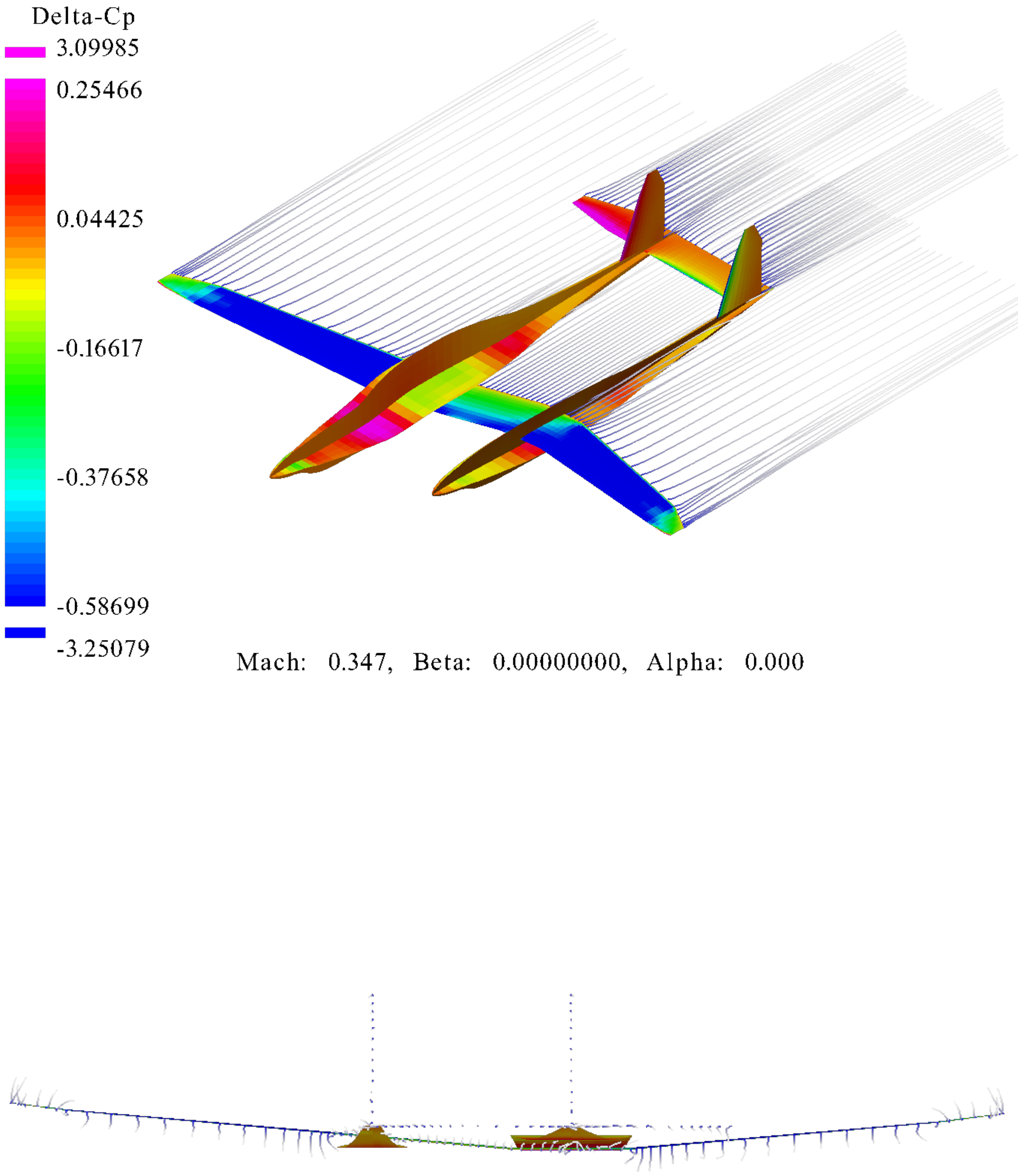

Figure 3.15 - Pressure distribution, trailing wakes for $\delta_f = 20°$ *at* $\alpha = 0°$ *and* $\beta = 0°$

3.3.2 *Lift coefficient*

For the WBT set, the analysis yields the following values for the *lift coefficient* (C_L).

	0°	**10°**	**20°**
$\boldsymbol{C_L}$	0,16	0,38	0,58

Table 3.7 - C_L values vs δ_f° at $\alpha = 0$°

By plotting the given values of C_L w.r.t. δ_f , we obtain:

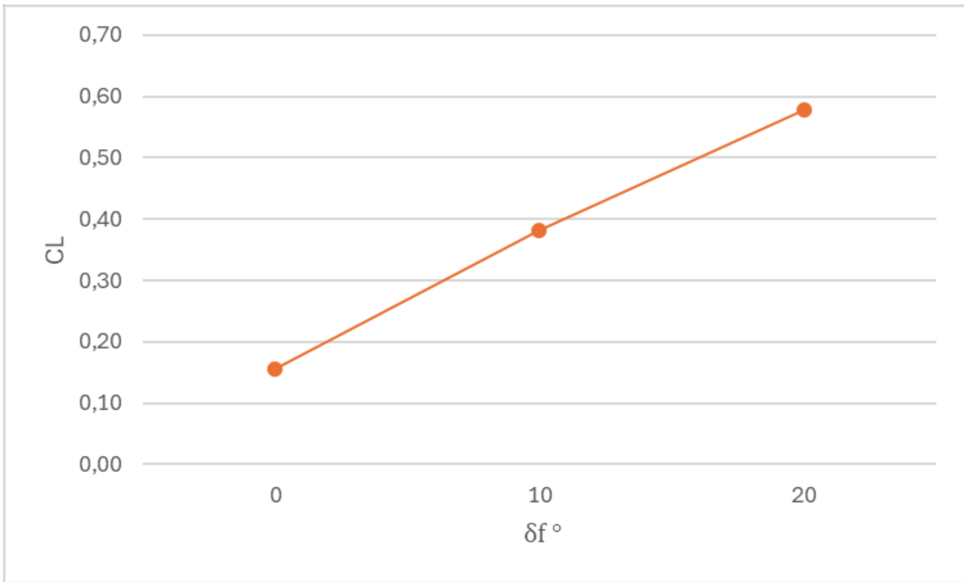

Figure 3.16 - C_L vs δ_f° at $\alpha = 0$°

A positive symmetric deflection of the flaperons causes an increase of C_L.

The control derivative of C_L w.r.t. δ_f is:

$$C_{L\delta_f} = 0{,}0211 \text{ deg}^{-1} \tag{3.4}$$

3.3.3 *Pitching moment coefficient*

For the WBT set, the analysis yields the following values for the *pitching moment coefficient* (C_{My}).

	0°	**10°**	**20°**
$\boldsymbol{C_{My}}$	-0,006	-0,094	-0,177

Table 3.8 - C_{My} values vs δ_f° at $\alpha = 0$°

By plotting the given values of C_{My} w.r.t. δ_f, we obtain:

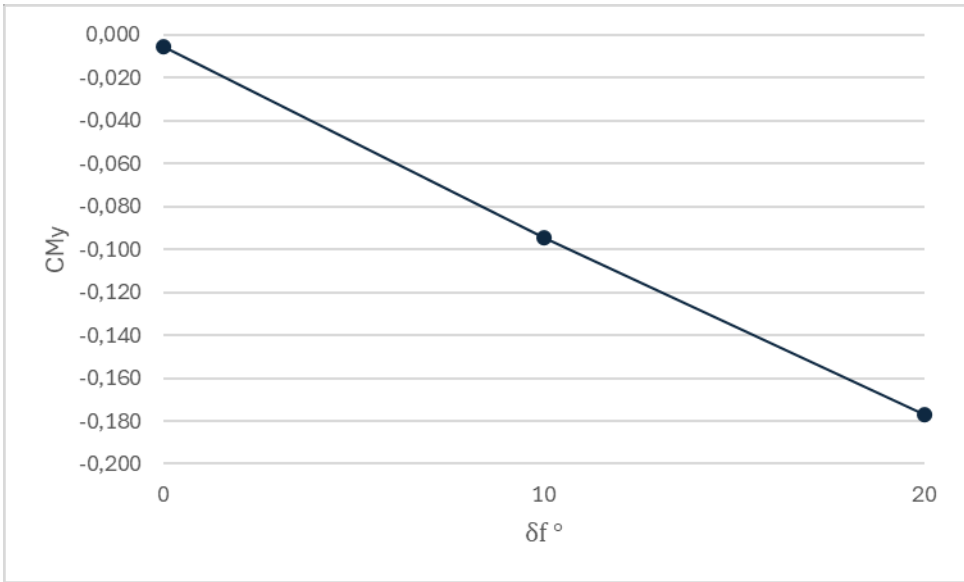

Figure 3.17 - C_{My} vs δ_f° at $\alpha = 0°$

A positive symmetric deflection of the flaperons causes an increase in magnitude of the negative pitching moment, meaning a greater tendency of the aircraft to dive.

The control derivative of C_{My} w.r.t. δ_f is:

$$C_{M\delta_f} = -0{,}0086 \text{ deg}^{-1} \tag{3.5}$$

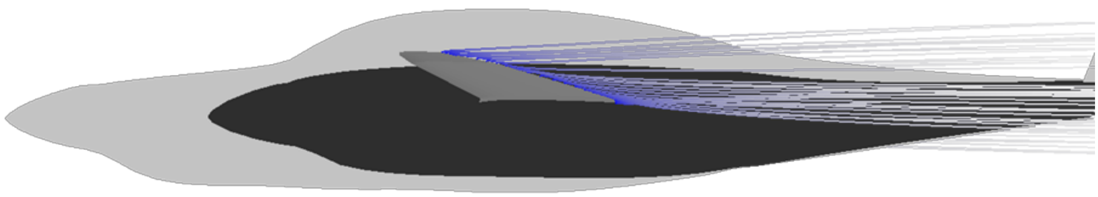

Figure 3.18 - Left view of trailing wakes for $\delta_f = 20°$ at $\alpha = 0°$ and $\beta = 0°$

3.4 Elevator effects on longitudinal aerodynamics

For this analysis, control surfaces have a deflection set to zero, except for the elevator. The elevator deflection angle (δ_e) interval considered is from $-20°$ to $10°$ with a step of $10°$. The angle of attack α and sideslip angle β are fixed at $0°$.

3.4.1 Lift coefficient

For the WBT set, the analysis yields the following values for the *lift coefficient* (C_L).

	$-20°$	$-10°$	$0°$	$10°$
C_L	-0,04	0,05	0,16	0,27

Table 3.9 - C_L values vs $\delta_e°$ at $\alpha = 0°$

By plotting the given values of C_L w.r.t. δ_e, we obtain:

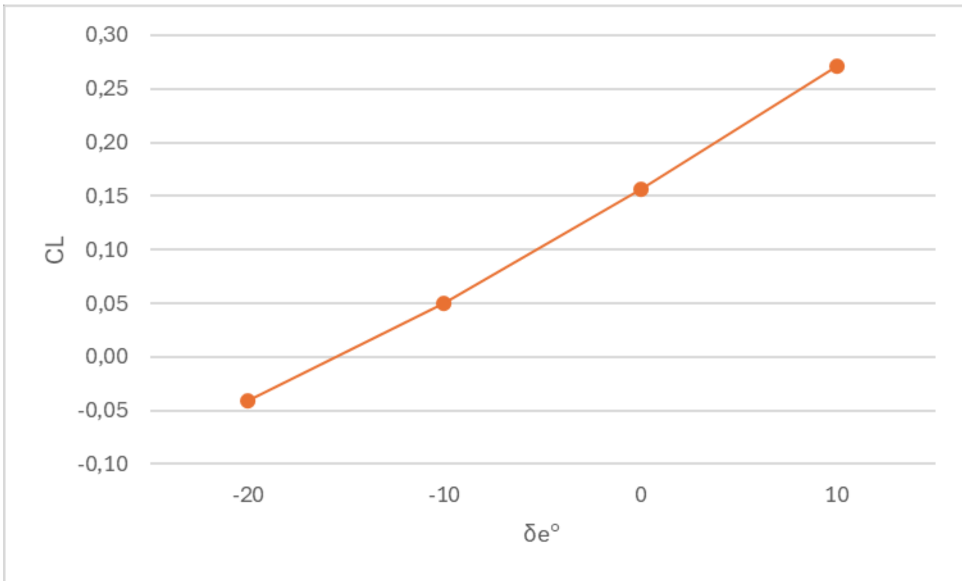

Figure 3.19 - C_L and vs $\delta_e°$ at $\alpha = 0°$

A negative deflection of the elevator causes a decrease of C_L, as the curvature of the horizontal tailplane becomes negative, hence generating negative lift.

The control derivative of C_L w.r.t. δ_e is:

$$C_{L\delta_e} = 0{,}0104 \, deg^{-1} \tag{3.6}$$

3.4.2 Pitching moment coefficient

For the WBT set, the analysis yields the following values for the *pitching moment coefficient* (C_{My}).

	$-20°$	$-10°$	$0°$	$10°$
C_{My}	1,515	0,806	-0,006	-0,886

Table 3.10 - C_{My} values vs δ_e° at $\alpha = 0°$

By plotting the given values of C_{My} w.r.t. δ_e, we obtain:

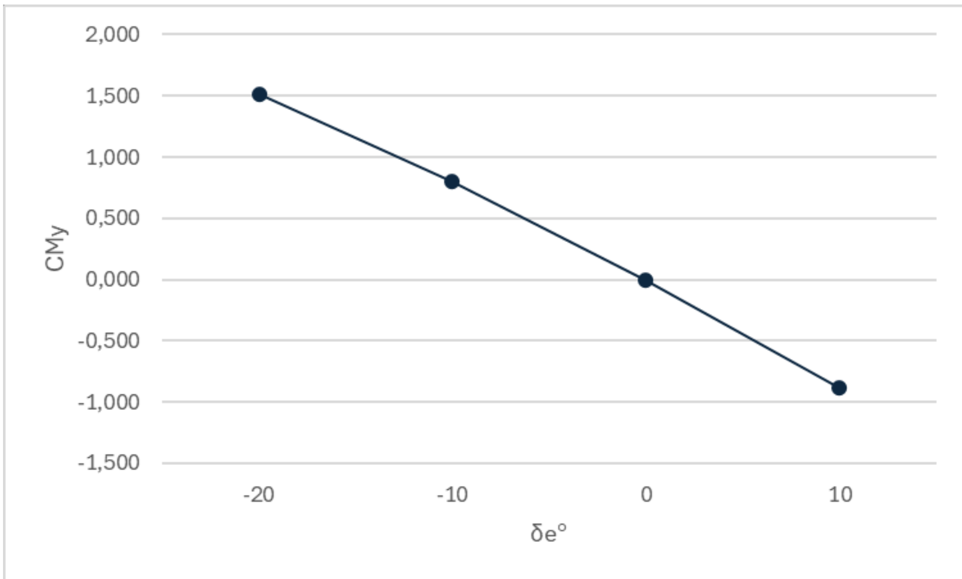

Figure 3.20 - C_{My} vs δ_e° at $\alpha = 0°$

A negative deflection of the elevator causes an increase of C_{My}, this derives from the given orientation to the control surface's rotation.

The control derivative of C_{My} w.r.t. δ_e is:

$$C_{My\delta_e} = -0{,}0801\ deg^{-1} \tag{3.7}$$

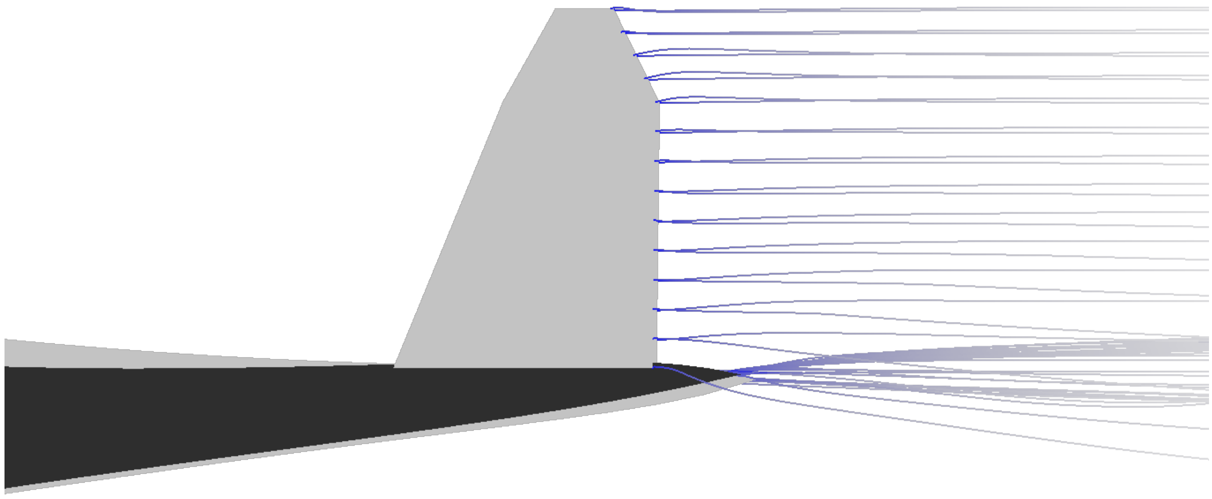

Figure 3.21 - Trailing wakes for $\delta_e = -20°$ at $\alpha = 0°$

3.5 Longitudinal static equilibrium and stability considerations

3.5.1 Linearized aerodynamic coefficients

In the hypothesis of small angle variations, aerodynamic coefficients, relative to longitudinal motion, can be expressed as follows:

$$C_L = C_{L0} + C_{L\alpha} \cdot \alpha + C_{L\delta_f} \cdot \delta_f + C_{L\delta_e} \cdot \delta_e \quad (3.8)$$

$$C_{My} = C_{My0} + C_{My\alpha} \cdot \alpha + C_{My\delta_f} \cdot \delta_f + C_{My\delta_e} \cdot \delta_e \quad (3.9)$$

where α, δ_f, δ_e are inputs and the remaining coefficients have been calculated through VSPAERO:

C_{L0}	C_{My0}	$C_{L\alpha}$	$C_{My\alpha}$
0,156	−0,0056	0,1107	−0,1198
$C_{L\delta_f}$	$C_{M\delta_f}$	$C_{L\delta_e}$	$C_{My\delta_e}$
0,0211	−0,0086	0,0104	−0,0801

Table 3.11 - Longitudinal residual terms and aerodynamic derivatives (deg^{-1})

3.5.2 Stability Margin and Neutral Point

Stability Margin, which is the distance between the aircraft center of gravity and neutral point, expressed as percentage of the mean chord $\bar{c}$, can be calculated as follows:

$$SM = \frac{C_{My\alpha}}{C_{L\alpha}} = -1{,}0822 \tag{3.10}$$

A negative value of SM implies that the aircraft is statically stable. This means that the center of gravity aft of the neutral point. The latter has the following X coordinate w.r.t. the body axes:

$$x_N = x_G - SM \cdot \bar{c} = 12{,}7598 \tag{3.11}$$

where x_G is the x coordinate of the center of gravity and $\bar{c}$ is the mean chord calculated by Open VSP.

3.5.3 Trim values

By solving the system of equations composed by Equation 3.7 and Equation 3.8, with $C_{My} = 0$ and $\delta_f = 0°$**,** the following expressions can be obtained:

$$\alpha_e = \frac{C_{Le} - C_{L0}}{C_{L\alpha}} \tag{3.11}$$

$$\delta_{ee} = -\frac{C_{My0} + C_{My\alpha} \cdot \alpha_e}{C_{My\delta_e}} \tag{3.12}$$

where α_e and δ_{ee} are respectively the angle of attack and the elevator deflection that allow a trimmed flight. The following table shows α_e and δ_{ee} varying with C_{Le}.

C_{Le}	α_e	δ_{ee}
0	-1,4	2,0
0,25	0,8	-1,3
0,5	3,1	-4,7
0,75	5,4	-8,1
1	7,6	-11,5
1,25	9,9	-14,9
1,5	12,1	-18,2

Table 3.12 - α_e° and δ_{ee}° values vs C_{Le}

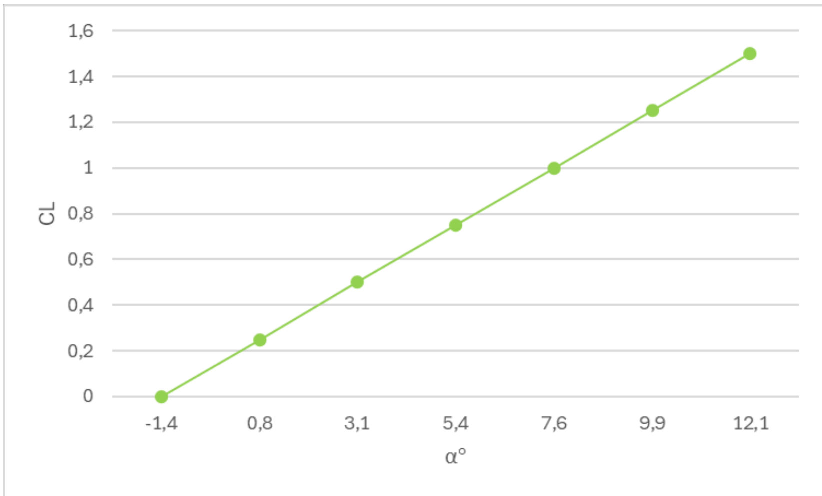

Figure 3.22 - C_{Le} vs α_e°

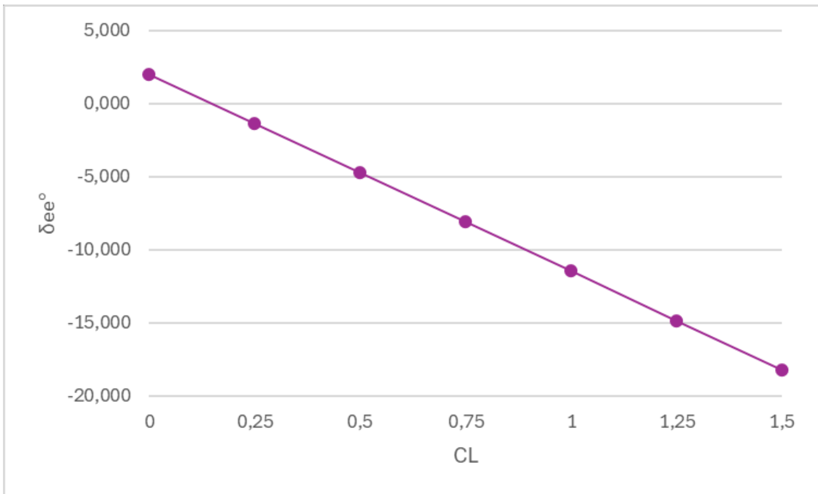

Figure 3.23 - δ_{ee}° vs C_{Le}

The derivative of C_{Le} w.r.t α_e is:

$$C_{Le\alpha_e} = 0{,}1107\ deg^{-1} \tag{3.13}$$

Whilst the derivative of δ_{ee} w.r.*t* C_L is:

$$\delta_{eeC_{Le}} = -13{,}5107\ deg \tag{3.14}$$

This last derivative can be also computed by the following formula:

$$\delta_{eeC_{Le}} = -\frac{C_{MyCL}}{C_{My\delta_e}} = -\frac{SM}{C_{My\delta_e}} \tag{3.15}$$

3.6 Longitudinal motion inputs and lateral-directional coefficients coupling

The following tables show how variations of α, δ_f and δ_e affects C_{Fy}, C_{Mz} and C_{Mx} (*sideforce coefficient*, *yawing moment coefficient*, and *rolling moment coefficient,* respectively).

$\boldsymbol{\alpha°}$	**0**	**2**	**4**	**6**	**8**	**10**	**12**
$\boldsymbol{C_{Fy}}$	0,00184	0,00550	0,00773	0,01131	0,01242	0,01299	0,01255
$\boldsymbol{C_{Mz}}$	−0,00034	0,00103	0,00244	0,00485	0,00661	0,00873	0,01091
$\boldsymbol{C_{Mx}}$	−0,00003	0,00300	0,00588	0,00888	0,01181	0,01558	0,01865

Table 3.13 - C_{Fy}, C_{Mz} and C_{Mx} values vs $\alpha°$ at $\beta = 0°$

C_{Mz} and C_{Mx} are linear w.r.t α with a positive slope having a magnitude of the order between 10^{-3} and 10^{-4}, meanwhile C_{Fy} is linear only in the α interval bracketed by 0° and 6°, with more or less the same slope of the other two coefficients.

$\boldsymbol{\delta_f°}$	**0**	**10**	**20**
$\boldsymbol{C_{Fy}}$	0,00184	0,00111	0,00037
$\boldsymbol{C_{Mz}}$	−0,00034	−0,00141	−0,0026
$\boldsymbol{C_{Mx}}$	−0,00003	0,00256	0,00482

Table 3.14 - C_{Fy}, C_{Mz} and C_{Mx} values vs $\delta_f°$ at $\alpha = 0°$, $\beta = 0°$

C_{Fy}, C_{Mz} and C_{Mx} are linear w.r.t δ_f with a slope having a magnitude of the order between 10^{-4} and 10^{-5}. It is positive for C_{Mx} and negative for the other two.

$\boldsymbol{\delta_e°}$	**−20**	**−10**	**0**	**10**
$\boldsymbol{C_{Fy}}$	-0,00349	-0,00115	0,00184	0,00539
$\boldsymbol{C_{Mz}}$	-0,00331	-0,00209	-0,00034	0,00144
$\boldsymbol{C_{Mx}}$	-0,00463	-0,00237	-0,00003	0,00307

Table 3.15 - C_{Fy}, C_{Mz} and C_{Mx} values vs $\delta_e°$ at $\alpha = 0°$, $\beta = 0°$

C_{Fy}, C_{Mz} and C_{Mx} are linear w.r.t δ_e with a positive slope having a magnitude of the order of 10^{-4}.

Since for C_{Fy}, C_{Mz} and C_{Mx}, a variation of α, δ_f and δ_e produces very small effects, it safe to say that longitudinal motion inputs and lateral-directional coefficients are strongly uncoupled, if not completely. This result aligns with Bryan's hypothesis [6].

4. Lateral-directional aerodynamic analysis

4.1 Analysis setup

4.1.1 Sets

The following sets have been defined for the lateral-directional aerodynamic analysis, to see how the coefficients vary from the isolated lifting surfaces to the complete aircraft. As for the longitudinal aerodynamic analysis, propellers and airducts have been neglected. The WBT set will still be referred to as the whole aircraft.

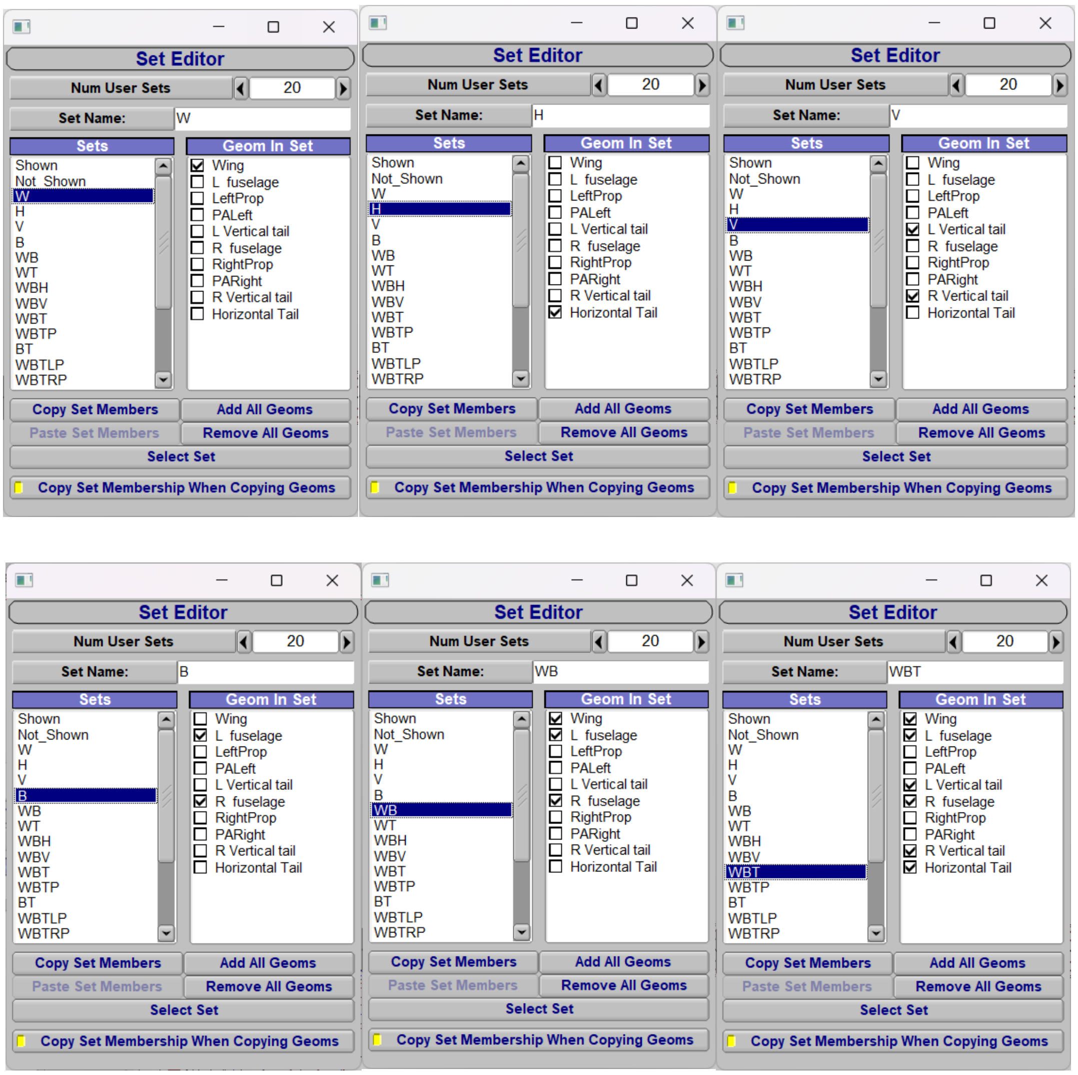

Figure 4.1 - Set editor tabs for lateral-directional analysis sets

4.2 Clean configuration

For this analysis, control surfaces have a deflection set to zero. The sideslip angle interval considered is from $\beta = -20°$ to $20°$ with a step of $4°$. The angle of attack (α) is fixed at $\alpha = 0°$.

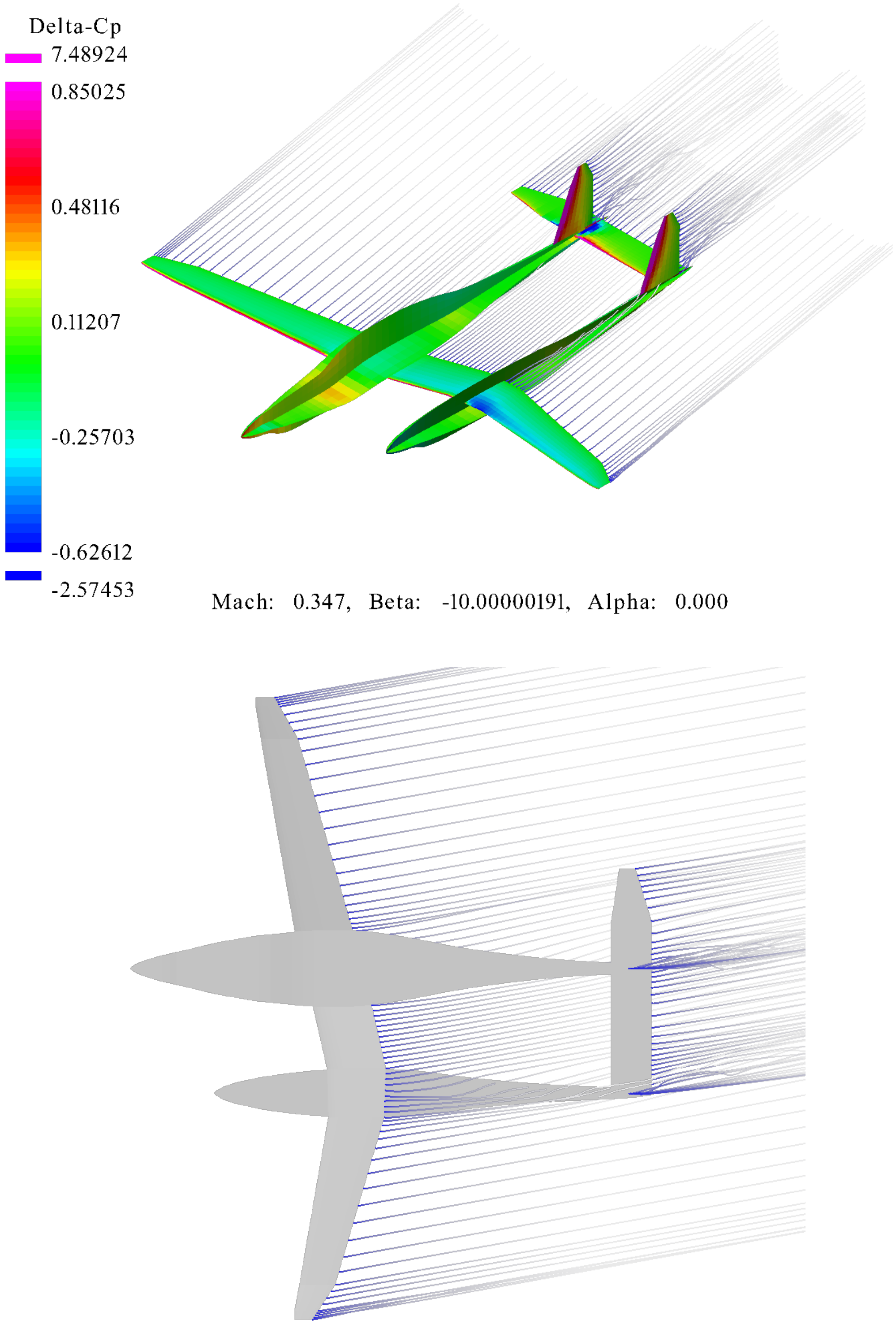

Figure 4.2 - Pressure distribution and trailing wakes for $\beta = -10°$ at $\alpha = 0°$

4.2.1 *Sideforce coefficient*

The analysis yields the following values for the *sideforce coefficient* (C_{Fy}).

$\beta°$	W	H	V	WB	WBT
-20	0,0135	0,0008	0,1778	0,0117	0,2184
-16	0,0116	0,0007	0,1454	0,0103	0,1781
-12	0,0096	0,0005	0,1110	0,0087	0,1362
-8	0,0074	0,0003	0,0750	0,0069	0,0915
-4	0,0051	0,0002	0,0379	0,0049	0,0469
0	0,0027	0,0000	0,0000	0,0029	0,0018
4	0,0003	-0,0002	-0,0379	0,0008	-0,0423
8	-0,0021	-0,0003	-0,0750	-0,0013	-0,0867
12	-0,0044	-0,0005	-0,1110	-0,0034	-0,1291
16	-0,0066	-0,0007	-0,1454	-0,0054	-0,1711
20	-0,0086	-0,0008	-0,1778	-0,0073	-0,2114

Table 4.1 - C_{Fy} values vs $\beta°$ at $\alpha = 0°$

By plotting the given values of C_{Fy} w.r.t. β, we obtain:

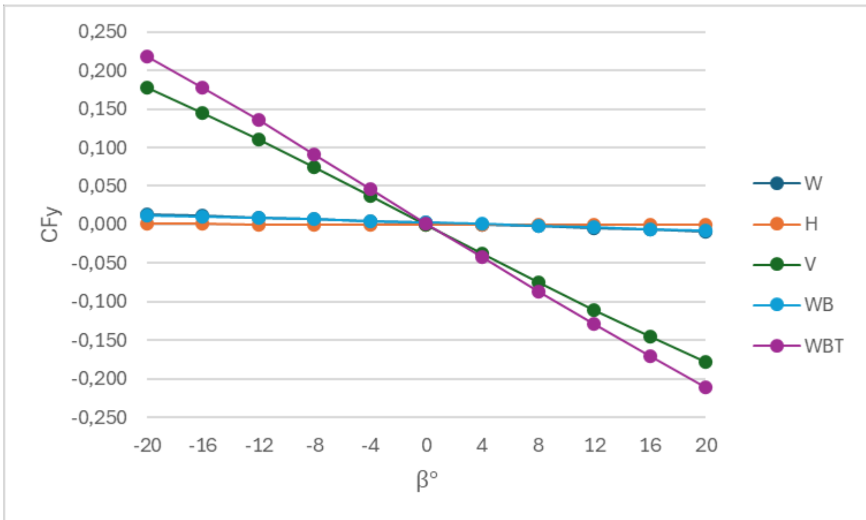

Figure 4.3 - C_{Fy} vs $\beta°$ at $\alpha = 0°$

The stability derivative of C_{Fy} w.r.t. β is:

$$C_{Fy\beta} = -0{,}0108961\, deg^{-1} \tag{4.1}$$

From theory, it is known that:

$$C_{Fy\beta} = C_{Fy\beta,WB} + C_{Fy\beta,H} + C_{Fy\beta,V} \tag{4.2}$$

It is possible to confirm that the contribution of the vertical tail is the most significant.

4.2.2 *Yawing moment coefficient*

The analysis yields the following values for the *yawing moment coefficient* (C_{Mz}).

$\beta°$	W	H	V	B	WB	WBT
-20	-0,0001	0,0003	0,0838	-0,0391	-0,0405	0,0605
-16	0,0000	0,0002	0,0687	-0,0322	-0,0336	0,0486
-12	0,0001	0,0001	0,0526	-0,0247	-0,0261	0,0375
-8	0,0002	0,0001	0,0356	-0,0168	-0,0180	0,0223
-4	0,0003	0,0000	0,0180	-0,0085	-0,0092	0,0108
0	0,0004	-0,0001	0,0000	0,0000	0,0002	-0,0003
4	0,0005	-0,0002	-0,0180	0,0084	0,0097	-0,0113
8	0,0005	-0,0003	-0,0359	0,0167	0,0188	-0,0240
12	0,0006	-0,0004	-0,0532	0,0247	0,0270	-0,0350
16	0,0006	-0,0005	-0,0699	0,0322	0,0347	-0,0479
20	0,0006	-0,0005	-0,0856	0,0391	0,0412	-0,0633

Table 4.2 - C_{Mz} values vs $\beta°$ at $\alpha = 0°$

By plotting the given values of C_{Mz} w.r.t. β, we obtain:

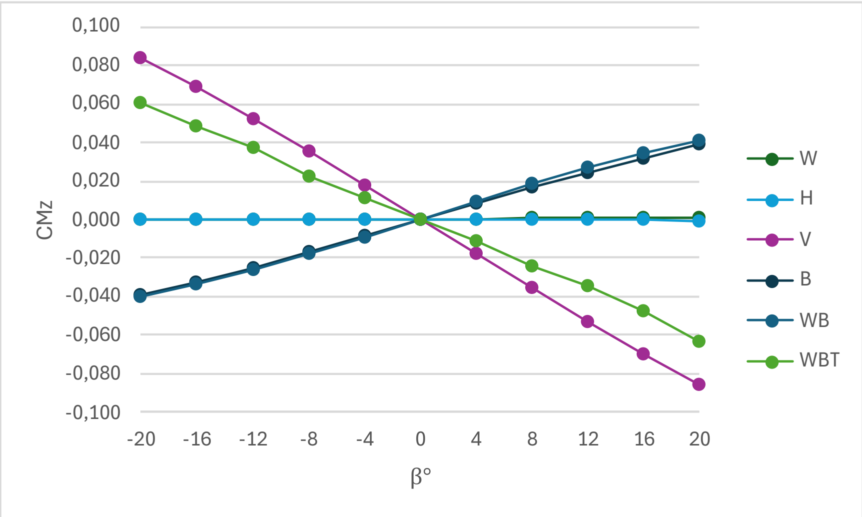

Figure 4.4 - C_{Mz} vs $\beta°$ at $\alpha = 0°$

The stability derivative of C_{Mz} w.r.t. β is:

$$C_{Mz\beta} = -0{,}0031456 \, deg^{-1} \tag{4.3}$$

To have stability, when a perturbation of the flow direction occurs, the aircraft reacts so it returns to the previous state. Since β is positive when the wind is coming from the right and the z axis is pointed downwards, for a positive β a negative C_{Mz} is needed so that the aircraft rotates towards the wind direction. Hence, when β increases, C_{Mz} must decrease. From theory, it is known that:

$$C_{Mz\beta} = C_{Mz\beta,B} + C_{Mz\beta,W} + C_{Mz\beta,V} \tag{4.4}$$

In Figure 4.4, it is possible to observe that the contribution of the fuselages is positive, that is unstable behavior, due to the free moments of a fusiform body. The second term is a function of the sweep angle. When β is nonzero, because of the negative sweep, the downwind wing generates more lift hence more induced drag that causes the aircraft to rotate away from the wind direction. Once again, the term related to the vertical tail dominates over the others. It takes to account the presence of a sidewash angle.

4.2.3 Rolling moment coefficient

The analysis yields the following values for the *rolling moment coefficient* (C_{Mx}).

$\beta°$	W	H	V	B	WB	WBT
-20	-0,0210	-0,0003	-0,0166	0,0014	-0,0183	-0,0321
-16	-0,0171	-0,0003	-0,0135	0,0012	-0,0150	-0,0275
-12	-0,0129	-0,0003	-0,0103	0,0010	-0,0113	-0,0215
-8	-0,0084	-0,0003	-0,0069	0,0008	-0,0076	-0,0152
-4	-0,0038	-0,0003	-0,0035	0,0006	-0,0035	-0,0079
0	0,0010	-0,0003	0,0000	0,0003	0,0009	0,0000
4	0,0058	-0,0003	0,0034	0,0001	0,0055	0,0084
8	0,0104	-0,0003	0,0068	-0,0001	0,0103	0,0171
12	0,0147	-0,0003	0,0100	-0,0003	0,0150	0,0259
16	0,0187	-0,0003	0,0130	-0,0005	0,0191	0,0348
20	0,0223	-0,0003	0,0158	-0,0006	0,0225	0,0405

Table 4.3 - C_{Mx} values vs $\beta°$ at $\alpha = 0°$

By plotting the given values of C_{Mx} w.r.t. β, we obtain:

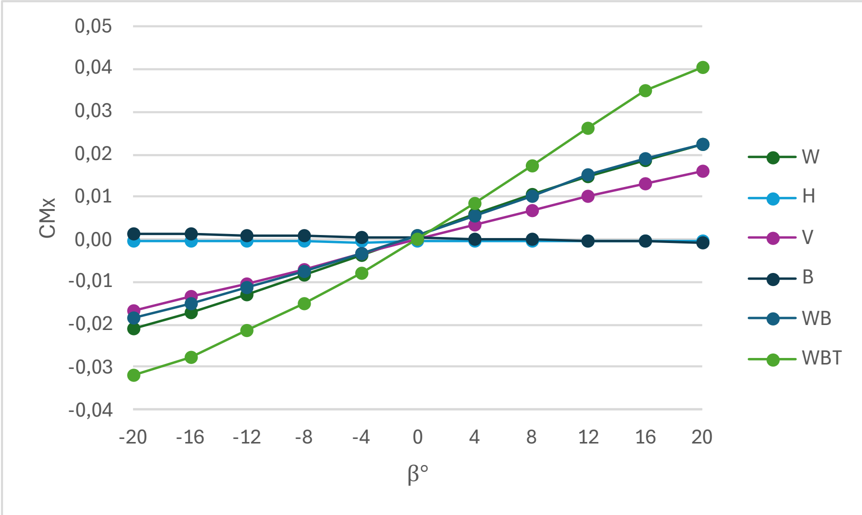

Figure 4.5 - C_{Mx} vs $\beta°$ at $\alpha = 0°$

The stability derivative of C_{Mx} w.r.t. β is:

$$C_{Mx\beta} = 0{,}0019208\, deg^{-1} \tag{4.5}$$

This is also known as the *dihedral effect*. Since β is positive when the wind is coming from the right and the x axis is pointed towards the rear, for a positive β, a positive C_{Mx} is needed so that the aircraft rolls towards the wind direction. Hence, when β increases, C_{Mx} must decrease. From theory, it is known that:

$$C_{Mx\beta} = C_{Mx\beta,WB} + C_{Mx\beta,H} + C_{Mx\beta,V} \tag{4.6}$$

In Figure 4.5, it is possible to observe that the first term is the most significant. It is a function of the sweep angle, the wing-fuselage relative positioning and the wing dihedral angle. The latter gives its name to the derivative. The second term is negligible w.r.t the others and the contribution of the vertical tail plane is due to the sideforce generated by β not aligned with the center of gravity's z coordinate.

4.3 Flaperon effects on lateral directional aerodynamics

For this analysis, control surfaces have a deflection set to zero, except for the flaperons acting as ailerons. The aileron deflection angle (δ_a) interval considered is from $-20°$ to $20°$ with a step of $10°$. The angle of attack α and sideslip angle β are fixed at $0°$.

4.3.1 Lifting surfaces loading

The following diagrams are the results of the analysis conducted on the WBT set.

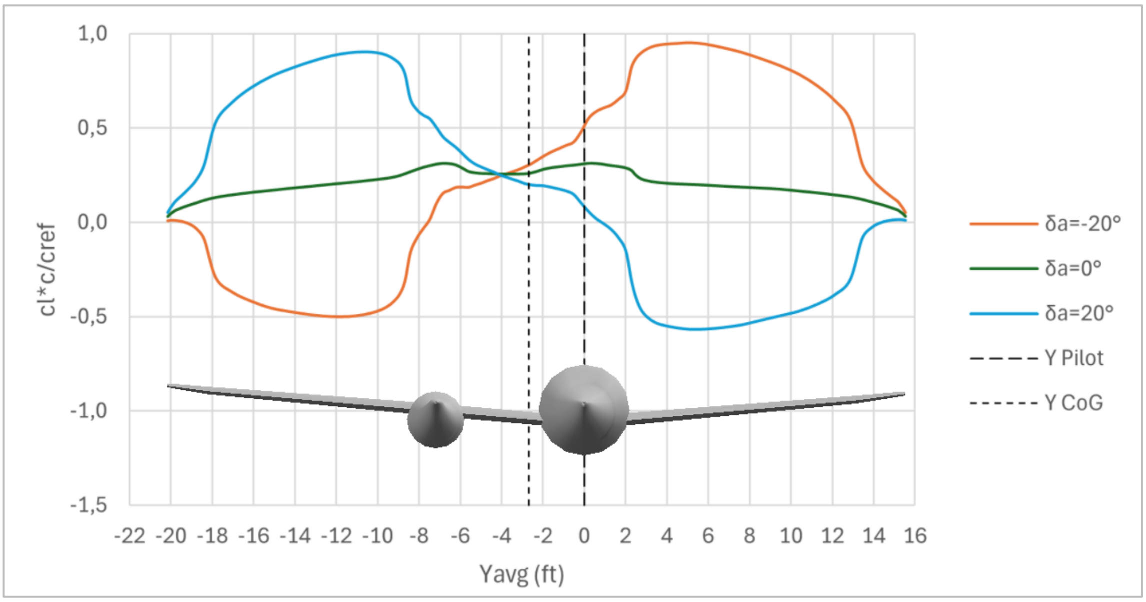

Figure 4.6 - Wing load distribution diagram varying with $\delta_a°$ at $\alpha = 0°$, $\beta = 0°$

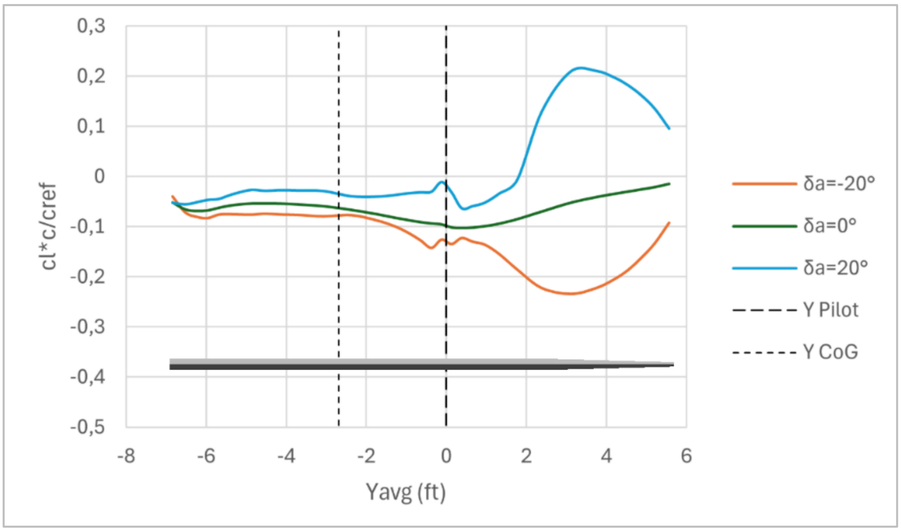

Figure 4.7 - Horizontal tail load distribution diagram varying with $\delta_a°$ at $\alpha = 0°$, $\beta = 0°$

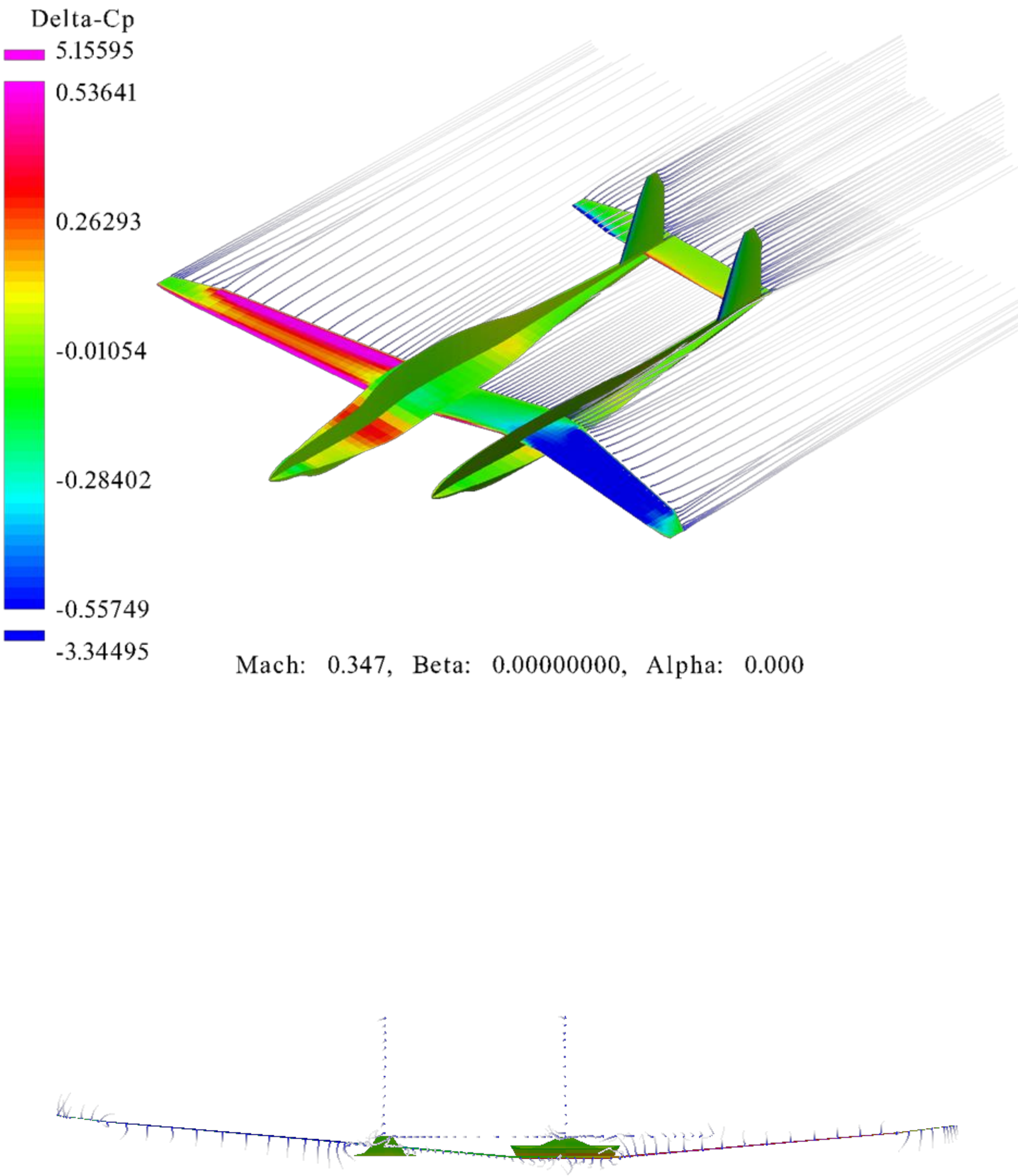

Figure 4.8 - Pressure distribution, trailing wakes for $\delta_a{}^\circ = 20^\circ$ at $\alpha = 0^\circ$, $\beta = 0^\circ$

4.3.2 Sideforce coefficient

For the WBT set, the analysis yields the following values for the *sideforce coefficient* (C_{Fy}).

	$-20°$	$-10°$	$0°$	$10°$	$20°$
$\mathbf{C_{Fy}}$	-0,0038	-0,0015	0,0018	0,0054	0,0087

Table 4.4 - C_{Fy} values vs δ_a° at $\alpha = 0°$, $\beta = 0°$

By plotting the given values of C_{Fy} w.r.t. δ_a , we obtain:

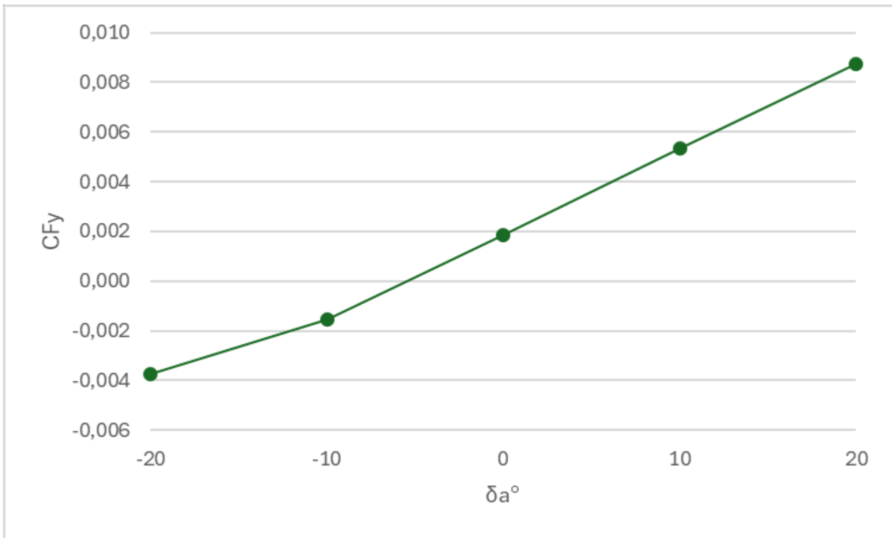

Figure 4.9 - C_{Fy} vs δ_a° at $\alpha = 0°$, $\beta = 0°$

The control derivative of C_{Fy} w.r.t. δ_a is:

$$C_{Fy\delta_\alpha} = 0{,}0003190\; deg^{-1} \tag{4.7}$$

The aileron deflection does not cause a significant variation of the sideforce, hence it is negligible w.r.t other derivatives.

4.3.3 Yawing moment coefficient

For the WBT set, the analysis yields the following values for the *yawing moment coefficient* (C_{Mz}).

	$-20°$	$-10°$	$0°$	$10°$	$20°$
$\mathbf{C_{Mz}}$	0,0084	0,0043	-0,0003	-0,0046	-0,0089

Table 4.5 - C_{Mz} values vs δ_a° at $\alpha = 0°$, $\beta = 0°$

By plotting the given values of C_{Mz} w.r.t. δ_a , we obtain:

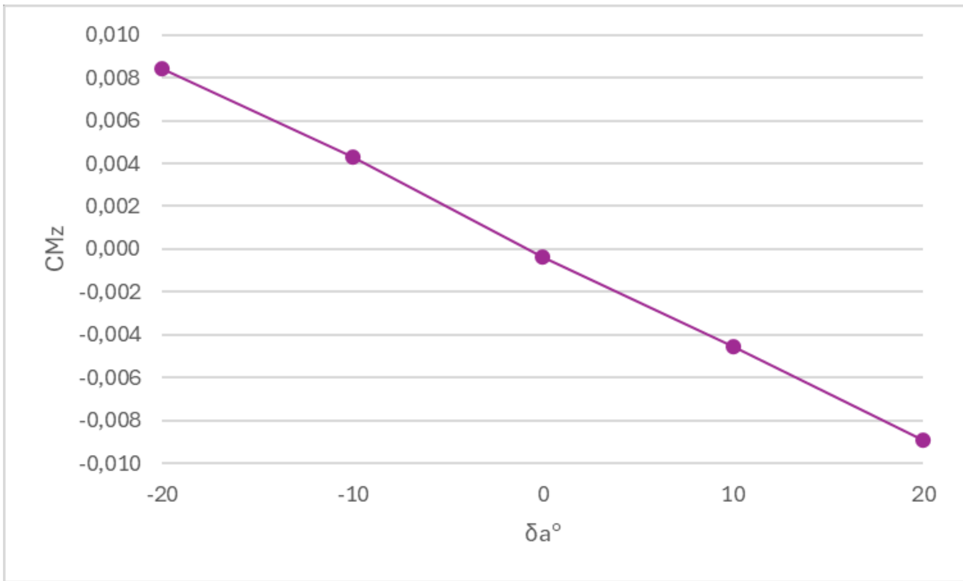

Figure 4.10 - C_{Mz} vs δ_a° at $\alpha = 0°,\ \beta = 0°$

The control derivative of C_{Mz} w.r.t. δ_a is:

$$C_{Mz\delta_\alpha} = -0{,}0004352\ deg^{-1} \tag{4.8}$$

This is also known as the *cross effect*. It is negative since when the ailerons are positively deflected (negative roll), the left wing generates more lift hence the induced drag increases, which makes the aircraft rotate to the left (negative yaw).

It is an unwanted effect, which can be alleviated or eliminated by compensating the difference of induced drag between the wings with a difference of parasite drag through differential rotation or frise ailerons. Note that for the aircraft of interest, this effect is already very small.

4.3.4 Rolling moment coefficient

For the WBT set, the analysis yields the following values for the *rolling moment coefficient* (C_{Mx}).

	$-20°$	$-10°$	$0°$	$10°$	$20°$
$\mathbf{C_{Mx}}$	0,0956	0,0512	0,0000	-0,0506	-0,0946

Table 4.6 - C_{Mx} values vs δ_a° at $\alpha = 0°,\ \beta = 0°$

By plotting the given values of C_{Mx} w.r.t. δ_a , we obtain:

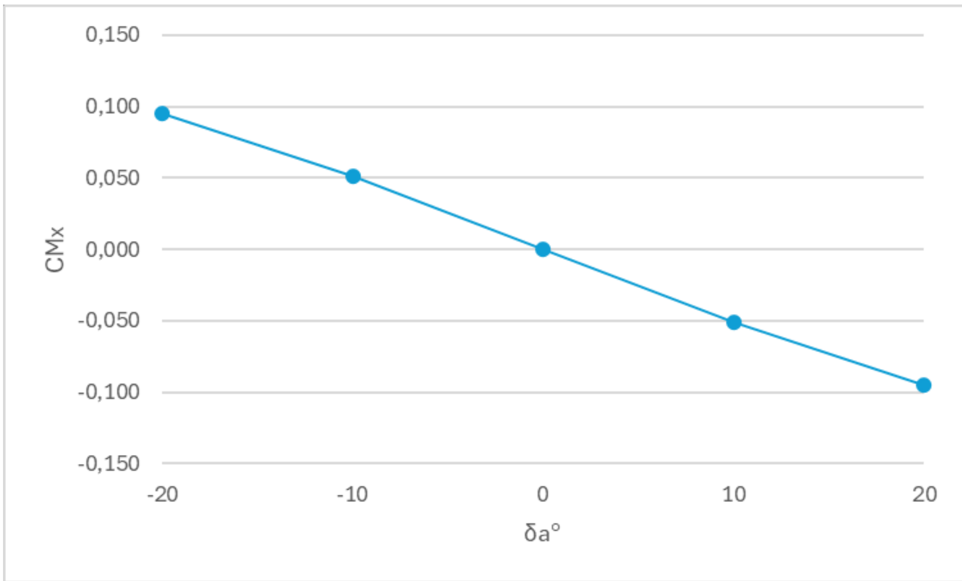

Figure 4.11 - C_{Mx} values vs δ_a° at $\alpha = 0°$, $\beta = 0°$

The control derivative of C_{Mx} w.r.t. δ_a is:

$$C_{Mx\delta_\alpha} = -0{,}0048214\ deg^{-1} \tag{4.9}$$

This is also known as *lateral control power*. This represents that aircraft's ability to rotate around the roll axis (x axis). It is negative since the orientation asymmetric deflection of the flaperons has been defined so that a positive deflection corresponds to negative roll.

4.4 Rudder effects on lateral directional aerodynamics

For this analysis, control surfaces have a deflection set to zero, except for the rudders. The rudder deflection angle (δ_r) interval considered is from $-20°$ to $20°$ with a step of $10°$. The angle of attack α and sideslip angle β are fixed at 0°.

4.4.1 Sideforce coefficient

For the WBT set, the analysis yields the following values for the *sideforce coefficient* (C_{Fy}).

	$-20°$	$-10°$	$0°$	$10°$	$20°$
$\mathbf{C_{Fy}}$	0,1375	0,0696	0,0018	-0,0689	-0,1327

Table 4.7 - C_{Fy} values vs δ_r° at $\alpha = 0°$, $\beta = 0°$

By plotting the given values of C_{Fy} w.r.t. δ_r , we obtain:

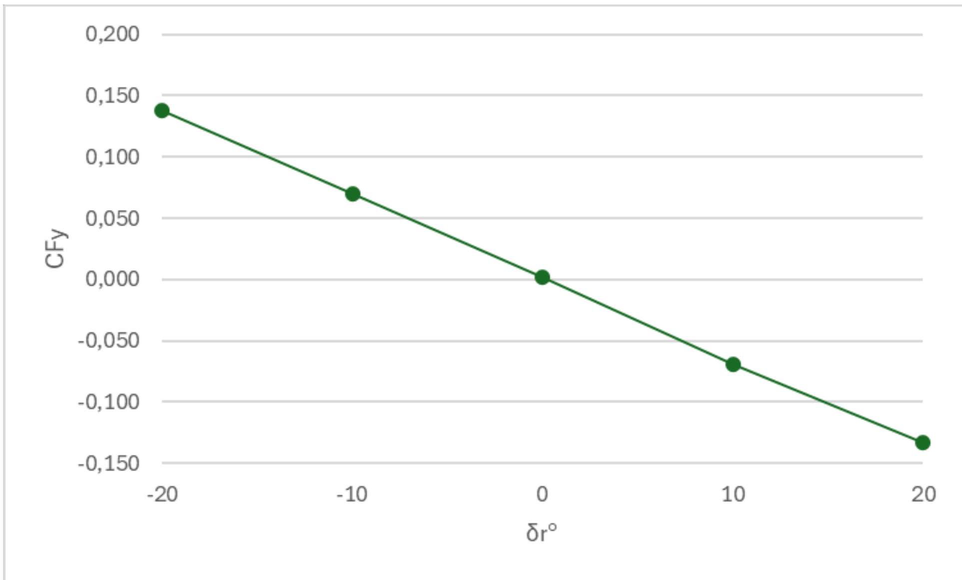

Figure 4.12 - C_{Fy} vs δ_r° at $\alpha = 0°$, $\beta = 0°$

A positive deflection (to the right) of the rudder generates a negative sideforce (to the left) due to the definition of its orientation w.r.t. the Open VSP reference frame.

The control derivative of C_{Fy} w.r.t. δ_r is:

$$C_{Fy\delta_r} = -0{,}0067893 \; deg^{-1} \tag{4.10}$$

4.4.2 Yawing moment coefficient

For the WBT set, the analysis yields the following values for the *yawing moment coefficient* (C_{Mz}).

	$-20°$	$-10°$	$0°$	$10°$	$20°$
$\mathbf{C_{Mz}}$	0,0602	0,0329	-0,0003	-0,0357	-0,0658

Table 4.8 - C_{Mz} values vs δ_r° at $\alpha = 0°,\ \beta = 0°$

By plotting the given values of C_{Mz} w.r.t. δ_r , we obtain:

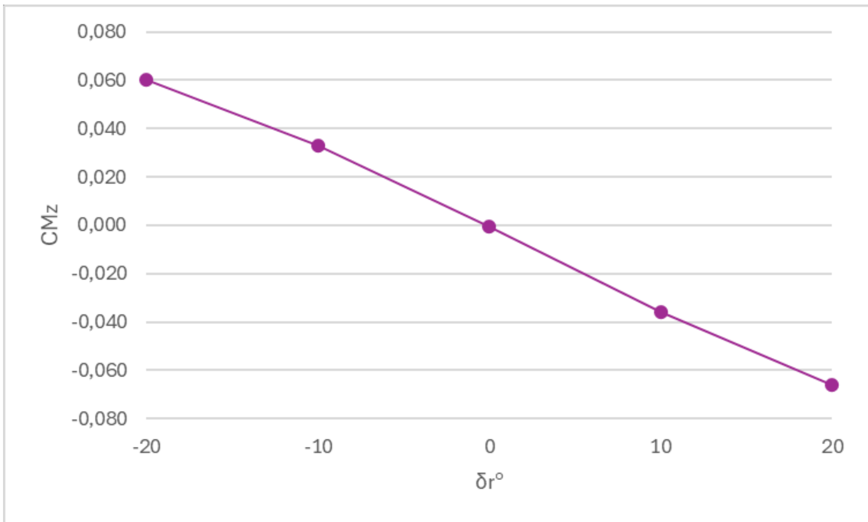

Figure 4.13 - C_{Mz} vs δ_r° at $\alpha = 0°,\ \beta = 0°$

The control derivative of C_{Mz} w.r.t. δ_r is:

$$C_{Mz\delta_r} = -0{,}0032058\,deg^{-1} \tag{4.11}$$

This is also known as *directional control power*. It represents the aircraft's ability to rotate around the yaw axis (z axis). It is always negative since the orientation of the rudder's deflection has been defined so that a positive deflection corresponds to negative yaw.

4.4.3 Rolling moment coefficient

For the WBT set, the analysis yields the following values for the *rolling moment coefficient* (C_{Mx}).

	$-20°$	$-10°$	$0°$	$10°$	$20°$
$\mathbf{C_{Mx}}$	-0,0077	-0,0049	0,0000	0,0058	0,0108

Table 4.9 - C_{Mx} values vs δ_r° at $\alpha = 0°,\ \beta = 0°$

By plotting the given values of C_{Mx} w.r.t. δ_r , we obtain:

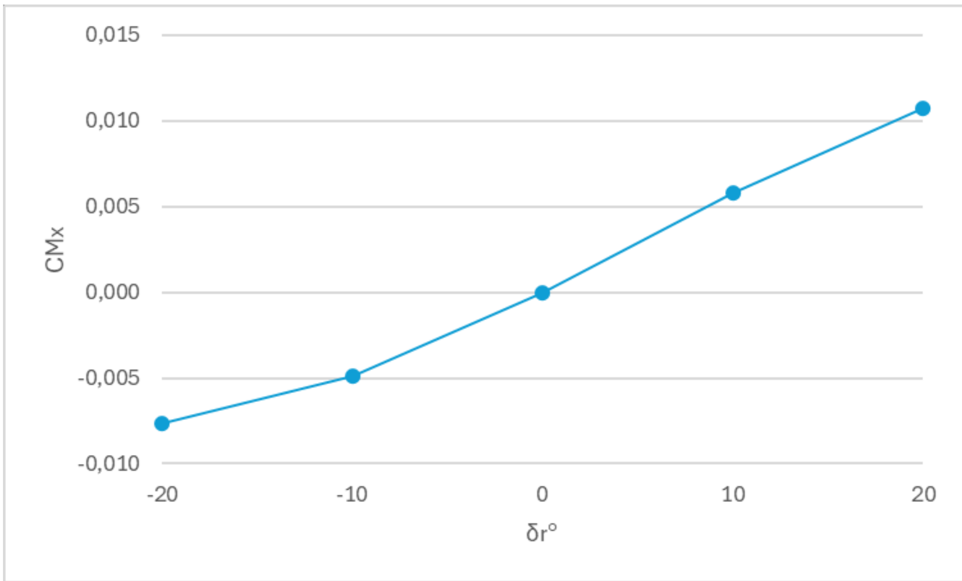

Figure 4.14 - C_{Mx} vs δ_r° at $\alpha = 0°$, $\beta = 0°$

The control derivative of C_{Mx} w.r.t. δ_r is:

$$C_{Mx\delta_r} = 0{,}0004753 \ deg^{-1} \tag{4.12}$$

This is also known as the *rudder induced roll*. When δ_r is positively deflected, the aircraft besides yawing negatively, rolls positively also. This effect depends on the attitude of the aircraft.

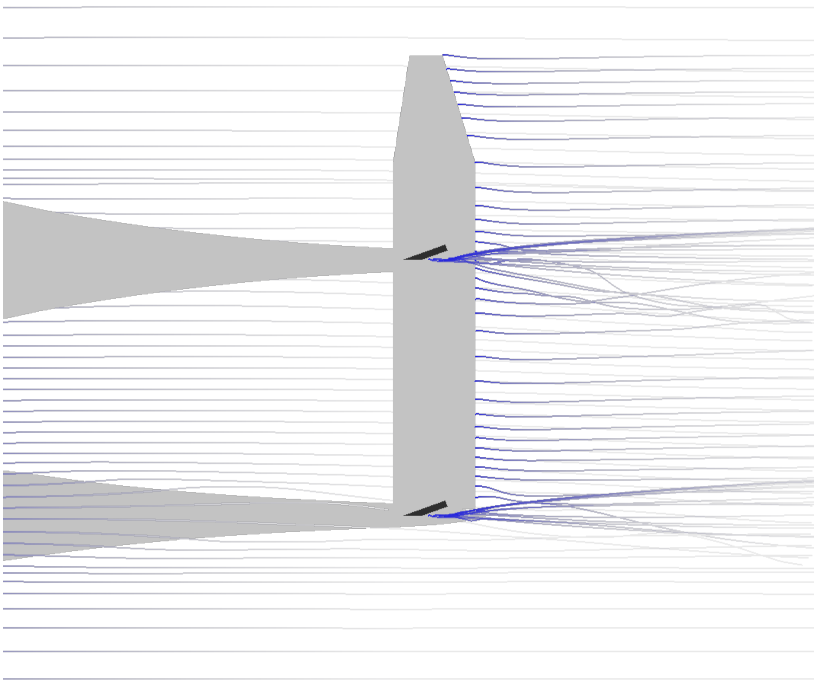

Figure 4.15 - Tail trailing wakes for $\delta_r = 20°$ at $\alpha = 0°$, $\beta = 0°$

4.5 Lateral-directional static equilibrium and stability considerations

4.5.1 Linearized aerodynamic coefficients

In the hypothesis of small angle variations, aerodynamic coefficients relative to lateral-directional motion can be expressed as follows:

$$C_{Fy} = C_{Fy0} + C_{Fy\beta} \cdot \beta + C_{Fy\delta_a} \cdot \delta_a + C_{Fy\delta_r} \cdot \delta_r \quad (4.13)$$

$$C_{Mz} = C_{Mz0} + C_{Mz\beta} \cdot \beta + C_{Mz\delta_a} \cdot \delta_a + C_{Mz\delta_r} \cdot \delta_r \quad (4.14)$$

$$C_{Mx} = C_{Mx0} + C_{Mx\beta} \cdot \beta + C_{Mx\delta_a} \cdot \delta_a + C_{Mx\delta_r} \cdot \delta_r \quad (4.15)$$

where β, δ_a, δ_r are inputs and the remaining coefficients have been calculated through VSPAERO:

C_{Fy0}	C_{Mz0}	C_{Mx0}
0,0018	−0,0003	0,0000
$C_{Fy\beta}$	$C_{Mz\beta}$	$C_{Mx\beta}$
−0,0108961	−0,0031456	0,0019208
$C_{Fy\delta_\alpha}$	$C_{Mz\delta_\alpha}$	$C_{Mx\delta_\alpha}$
0,0003190	−0,0004352	−0,0048214
$C_{Fy\delta_r}$	$C_{Mz\delta_r}$	$C_{Mx\delta_r}$
−0,0067893	−0,0032058	0,0004753

Table 4.10 - Lateral directional residual terms and aerodynamic derivatives (deg^{-1})

Note that some residual terms (C_{Fy0}, C_{Mz0}) are nonzero due to the asymmetricity of the aircraft. Overall, as already discussed, the aircraft is lateral-directionally stable.

4.6 Lateral-directional inputs and longitudinal coefficients coupling

The following tables show how variations of β, δ_a and δ_r affects C_L and C_{My}.

$\boldsymbol{\beta°}$	-20	10	0	10	20
$\boldsymbol{C_L}$	0,29057	0,19693	0,15619	0,14046	0,16720
$\boldsymbol{C_{My}}$	-0,72915	-0,19729	-0,00558	0,05739	-0,04755

Table 4.11 - C_L and C_{My} values vs $\beta°$ at $\alpha = 0°$

At around $\beta = 10°$, C_L has a minimum and C_{My} has a maximum. The greater β, the greater are C_L and C_{My} variations; the latter can reach an order of magnitude higher. C_{My}'s value for $\beta = -20°$ is quite odd and hard to justify, although this result is due to the software limitations, unable to manage trailing wakes interaction with aircraft parts in the best way.

$\boldsymbol{\delta_a}$ °	**-20**	**10**	**0**	**10**	**20**
$\boldsymbol{C_L}$	0,16997	0,16547	0,15619	0,14256	0,13111
$\boldsymbol{C_{My}}$	0,28534	0,16334	-0,00558	-0,17409	-0,34230

Table 4.12 - C_L and C_{My} values vs δ_a° at $\alpha = 0°$, $\beta = 0°$

C_L and C_{My} are linear w.r.t δ_a, with a negative slope having a magnitude of the order between 10^{-2} and 10^{-3}.

$\boldsymbol{\delta_r}$ °	**-20**	**10**	**0**	**10**	**20**
$\boldsymbol{C_L}$	0,22268	0,17514	0,15619	0,16047	0,18555
$\boldsymbol{C_{My}}$	-0,33372	-0,10754	-0,00558	0,01383	-0,00768

Table 4.13 - C_L and C_{My} values vs δ_r° at $\alpha = 0°$, $\beta = 0°$

At around $\delta_r = 0°$, C_L has a minimum, meanwhile at around $\delta_r = 10°$ C_{My} has a maximum. C_L and C_{My} trends w.r.t. δ_r are like those w.r.t β. Despite having a change of C_L by rotating the rudder seems unphysical because of the aft position of the rudder, this should make sense by observing that a rotation of the rudder generates a yawing moment that changes the sideslip angle β seen by the wing. This also explains the similarity between the said trends. As before, the greater the δ_r, the greater are C_L and C_{My} variations, that can increase until two orders of magnitude for the latter.

For C_L and C_{My}, small variations of β, δ_a and δ_r still produce small effects, although they increase as the variations get bigger; in particular, the effects are more felt by C_{My}. These results tell us that for this specific aircraft, it is not completely true that lateral-directional inputs are uncoupled with longitudinal aerodynamic coefficients, as Bryan's hypothesis suggests. Nevertheless, this behavior can also be found in conventional symmetric aircraft and the coupling remains very loose.

5. Propulsive effects

5.1 Analysis setup

5.1.1 Sets

For the following analysis, the following sets have been defined. As before, airducts have been neglected for the analysis.

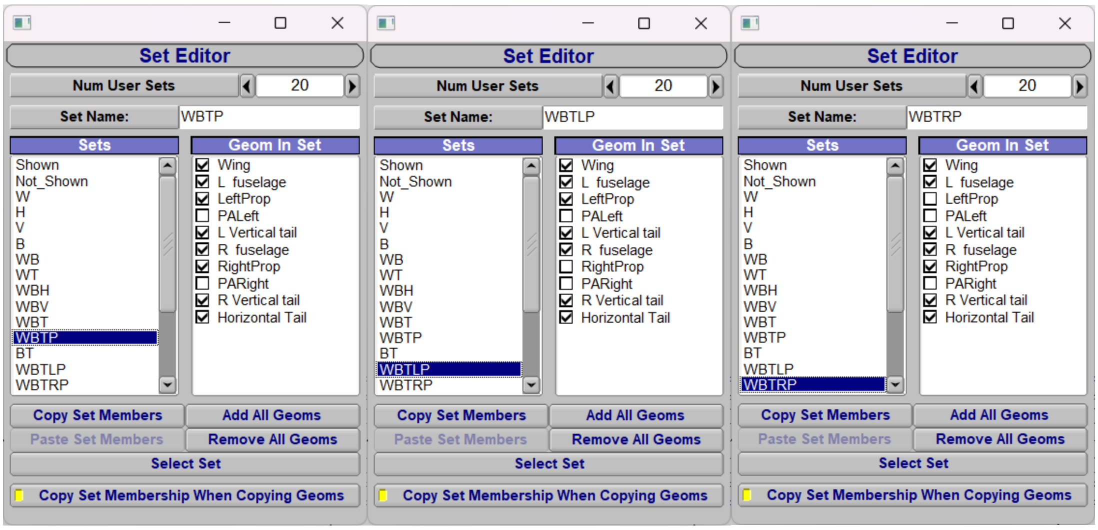

Figure 5.1 - Set editor tabs for propulsive effects analysis

5.1.2 Engine configurations

To address asymmetric thrust issues, propellers have been modelled as disk actuators. The following configurations have been studied.

- Both engine on, at 50% power (WBTP set), that is the economic cruise case.
- Left engine on, at 100% power, right engine off (WBTLP set), in case of a right engine failure.
- Right engine on, at 100% power, left engine off (WBTRP set), in case of a left engine failure.

Results have been compared to the ones obtained with the WBT set, that is the whole aircraft without propeller and airducts.

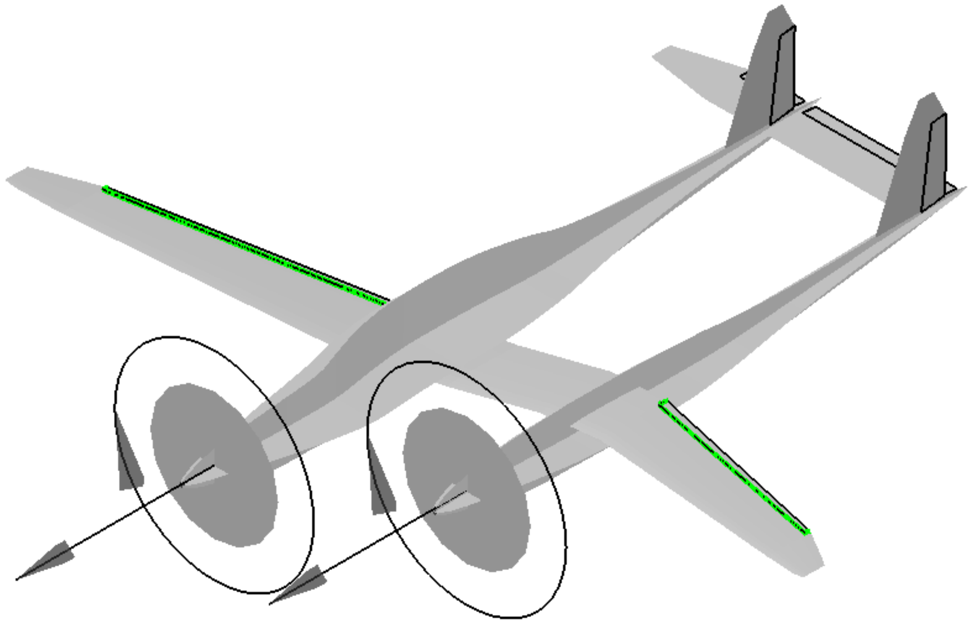

Figure 5.2 - VLM Geometry preview for the WBTP set

5.1.3 Disk actuators parameters

From the aircraft and engine specifications, the following parameters have been collected:

	Left engine	**Right engine**
Name	$Lyc\ TIO - 360A1B$	$Lyc\ TIO - 360C1A6D$
Shaft Power (P_S)	$200\ hp$	$210\ hp$
Max RPM	2575	2575

Table 5.1 - Engine specifications

From the drawing, the propeller diameter D measurement is $6{,}1\ ft$. A propeller efficiency η has been hypothesized to be 0,85. To completely set up the analysis, the thrust coefficient and power coefficient are needed. They are defined as follows.

$$C_T = \frac{T}{\rho \cdot n^2 \cdot D^4} \tag{5.1}$$

$$C_P = \frac{P_S}{\rho \cdot n^3 \cdot D^5} \tag{5.2}$$

Where T is required thrust, P_S is shaft power, ρ is the air density, n is the number of revolutions per second, and D is the propeller diameter. The two are related through the following formula:

$$C_P = J \cdot \frac{C_T}{\eta} \tag{5.3}$$

Where J is the advance ratio, which is defined, given the flight velocity V, as:

$$J = \frac{V}{n \cdot D} \tag{5.4}$$

Starting from the power conditions observed in engine specifications, C_P has been calculated, C_T , follows from Equation (5.4). n and P_S are hypothesized linearly proportional. For each configuration, the following parameters have been computed.

	Left Engine				**Right engine**			
	n	J	C_T	C_P	n	J	C_T	C_P
WBTP	21,458	2,708	0,187	0,597	21,458	2,708	0,187	0,626
WBTLP	42,917	1,354	0,094	0,149	/	/	/	/
WBTRP	/	/	/	/	42,917	1,354	0,098	0,157

Table 5.2 - Propulsive effects analysis parameters

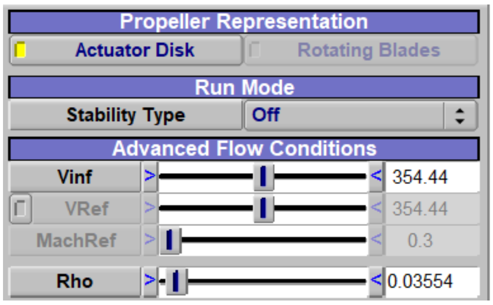

Figure 5.3 - VSPAERO Actuator disk set-up

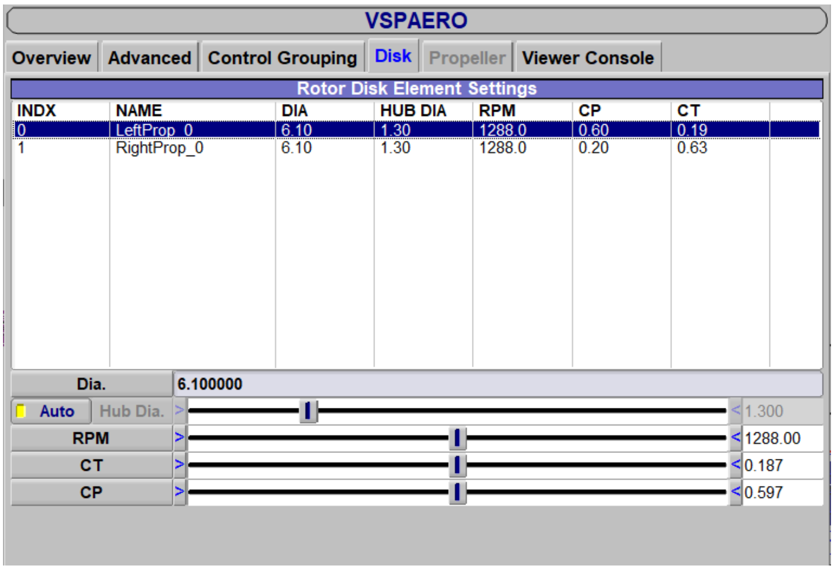

Figure 5.4 - VSPAERO Actuator Disk tab for WBTP set

5.2 Results

To observe the effects of asymmetric thrust, α and β have been fixed at 0°.

5.2.1 Lifting surfaces load distribution

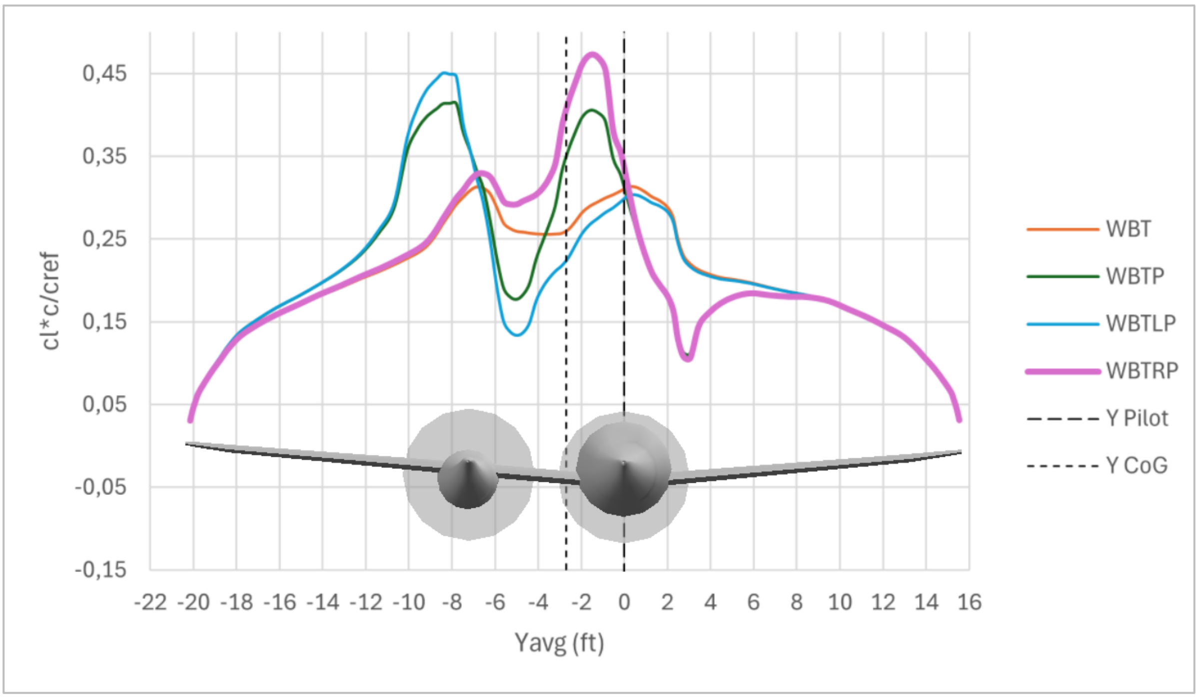

Figure 5.5 - Wing load distribution diagram for different engine configurations

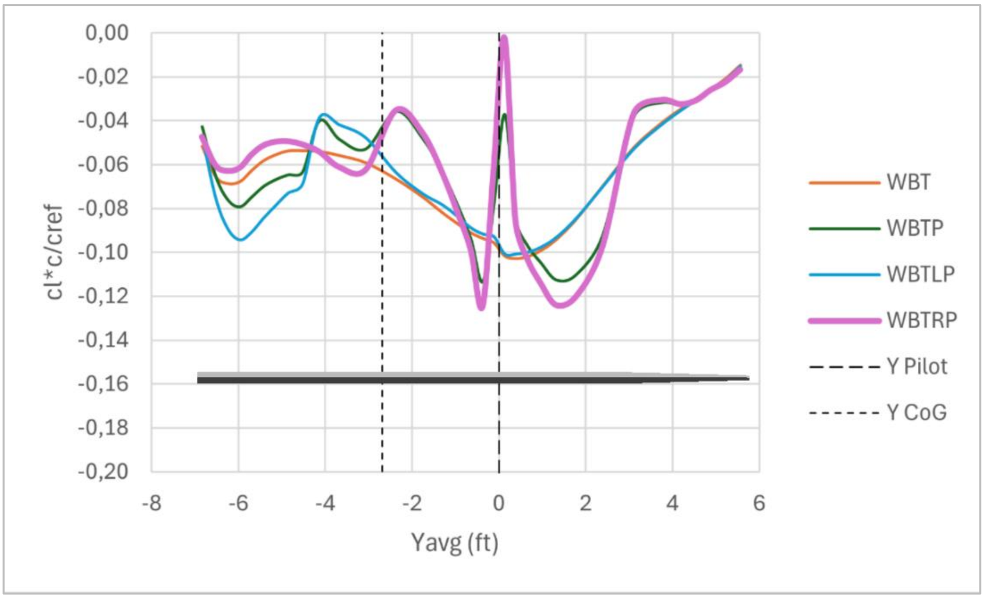

Figure 5.6 - Horizontal tail load distribution diagram for different engine configurations

5.2.2 Lift coefficient

WBT	$WBTP$	$WBTLP$	$WBTRP$
0,1562	0,1648	0,1627	0,1626

Table 5.3 - C_L for different engine configurations at $\alpha = 0°$, $\beta = 0°$

$WBTP$	$WBTLP$	$WBTRP$
5,48%	4,15%	4,08%

Table 5.4 - Percentage changes of C_L w.r.t. prop-off configuration (WBT)

5.2.3 Pitching moment coefficient

WBT	$WBTP$	$WBTLP$	$WBTRP$
-0,0056	-0,0245	-0,0090	-0,0214

Table 5.5 - C_{My} for different engine configurations at $\alpha = 0°$, $\beta = 0°$

$WBTP$	$WBTLP$	$WBTRP$
-0,0189	-0,0034	-0,0159

Table 5.6 - C_{My} relative difference w.r.t prop-off configuration (WBT)

5.2.4 Yawing moment coefficient

WBT	$WBTP$	$WBTLP$	$WBTRP$
-0,00034	0,00554	0,00175	0,00465

Table 5.7 - C_{Mz} for different engine configurations at $\alpha = 0°$, $\beta = 0°$

$WBTP$	$WBTLP$	$WBTRP$
0,00589	0,00209	0,00499

Table 5.8 - C_{Mz} relative difference w.r.t prop-off configuration (WBT)

5.2.5 Rolling moment coefficient

WBT	$WBTP$	$WBTLP$	$WBTRP$
0,0000	-0,0048	-0,0031	-0,0023

Table 5.9 - C_{Mx} for different engine configurations at $\alpha = 0°$, $\beta = 0°$

$WBTP$	$WBTLP$	$WBTRP$
-0,0047	-0,0031	-0,0022

Table 5.10 - C_{Mx} relative difference w.r.t prop-off configuration (WBT)

5.3 Propulsive effects considerations

By considering the propulsive effects, the linearized moment coefficients take the following expressions:

$$C_{My} = C_{My0} + C_{My\beta} \cdot \beta + C_{My\delta_a} \cdot \delta_a + C_{My\delta_r} \cdot \delta_r + \boldsymbol{C_{My,PE}} \tag{5.1}$$

$$C_{Mz} = C_{Mz0} + C_{Mz\beta} \cdot \beta + C_{Mz\delta_a} \cdot \delta_a + C_{Mz\delta_r} \cdot \delta_r + \boldsymbol{C_{Mz,PE}} \tag{5.2}$$

$$C_{Mx} = C_{Mx0} + C_{Mx\beta} \cdot \beta + C_{Mx\delta_a} \cdot \delta_a + C_{Mx\delta_r} \cdot \delta_r + \boldsymbol{C_{Mx,PE}} \tag{5.3}$$

$C_{My,PE}$, that is the propulsive effects on the pitching moment, has been computed by deducting the C_{My0} value obtained from the WBT set from C_{My}. In other words, it is the relative difference w.r.t the prop-off configuration (WBT), as shown in Table 5.6 - $\boldsymbol{C_{My}}$ relative difference w.r.t prop-off configuration (WBT). The same applies to the other terms in bold.

From Table 5.4, it is possible to affirm that C_L is negligibly affected by propulsive effects. However, the same cannot be said for the moment coefficients. The propellers contribute negatively to C_{My} , with an order of magnitude of 10^{-2} for both the both-engine-on and right-engine-on only configurations, while the contribution is an order of magnitude smaller for the left-engine-on only scenario. The propulsive effects on C_{Mz} are positive, with the right-engine-on only configuration being less than 15% of the both-engine-on, whereas the left-engine-on only configuration yields less than half the magnitude of the both-engines-on case. Lastly, the effects on C_{Mx} are negative and characterized by an order of magnitude of 10^{-3}. In comparison to the residual terms of the WBT set, all these propulsion-related effects are larger by one or two orders of magnitude. Propulsive effects are less pronounced when the aircraft is flying with only one engine. These results confirm that the aircraft is minimally impacted by asymmetrical thrust issues. Advance CFD software could be useful to make the precedent affirmation stronger, because of the limitations of the model and method of choice. A comparison with a light symmetric twin-engine is done in the next chapter.

6. Comparison with symmetric twin-engine aircraft

6.1 Cessna 402

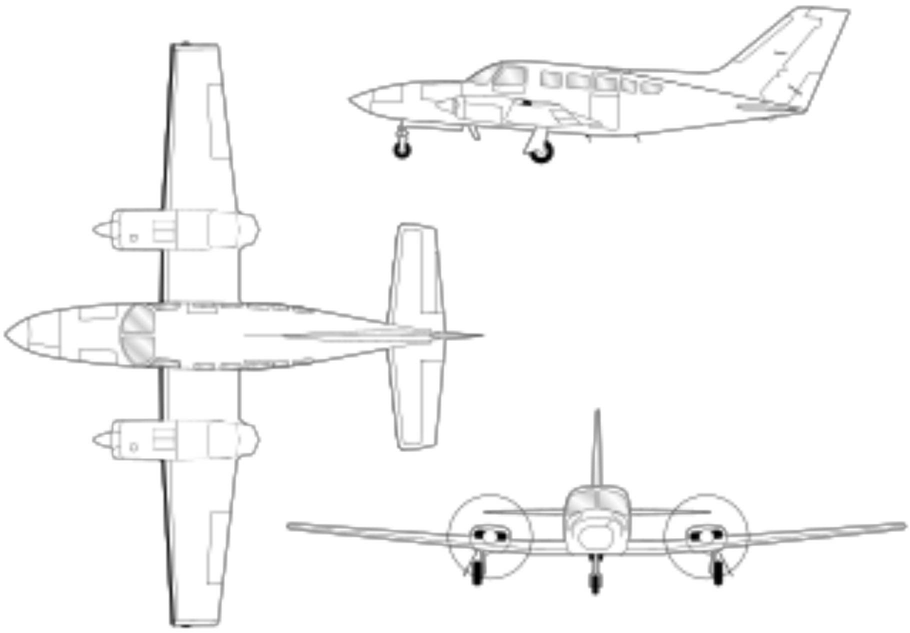

Figure 6.1 - Cessna 402 drawing

The Cessna 402 is a light twin-engine conventional aircraft, unlike the Rutan Boomerang. A model of the former is available in VSP Airshow. The same analyses have been conducted on this model to make a comparison possible. The selected flight condition remains economy cruise at 50% power.

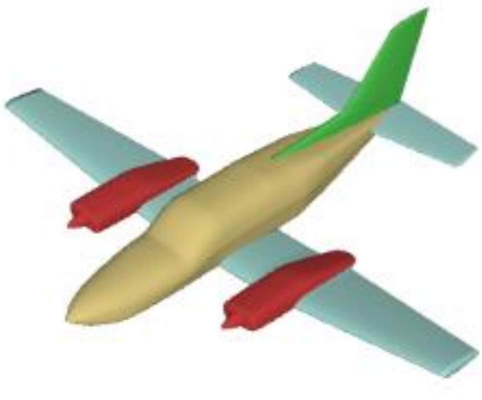

Figure 6.2 - Cessna 402 model taken from VSP Airshow

6.2 Rutan Boomerang vs Cessna 402C

6.2.1 Longitudinal aerodynamics

	Rutan Boomerang	Cessna 402
C_{L0}	0,156	-0,031
C_{My0}	−0,0056	0,1974
$C_{L\alpha}$	0,1107	0,0997
$C_{My\alpha}$	−0,1198	-0,0114
$C_{L\delta_e}$	0,0104	0,0118
$C_{My\delta_e}$	−0,0801	-0,0306

Table 6.1 - Longitudinal aerodynamic residual terms and derivatives (deg^{-1}) comparison

6.2.2 Lateral-directional aerodynamic residual terms and derivatives

	Rutan Boomerang	Cessna 402
C_{Fy0}	0,0018	0,0000
C_{Mz0}	−0,0003	0,0000
C_{Mx0}	0,0000	0,0000
$C_{Fy\beta}$	−0,0109	−0,0074
$C_{Mz\beta}$	−0,0031	−0,0015
$C_{Mx\beta}$	0,0019	0,0013
$C_{Fy\delta_\alpha}$	0,0003	0,0009
$C_{Mz\delta_\alpha}$	−0,0004	−0,0001
$C_{Mx\delta_\alpha}$	−0,0048	−0,0047
$C_{Fy\delta_r}$	−0,0068	−0,0039
$C_{Mz\delta_r}$	−0,0032	−0,0015
$C_{Mx\delta_r}$	0,0005	0,0003

Table 6.2 - Lateral-directional aerodynamic residual terms and derivatives (deg^{-1}) comparison

6.2.3 Propulsive effects

	Rutan Boomerang			Cessna 402	
	WBTP	***WBTLP***	***WBTRP***	***WBTP***	***WBT1P***
C_{My}	-0,0189	-0,0034	-0,0159	0,00517	0,00356
C_{Mz}	0,00589	0,00209	0,00499	0,00010	-0,00164
C_{Mx}	-0,0047	-0,0031	-0,0022	0,00002	-0,01176

Table 6.3 - Propulsive effects comparison

	Rutan Boomerang		Cessna 402
	WBTLP	***WBTRP***	***WBT1P***
C_{My}	-82%	-16%	-31%
C_{Mz}	-65%	-15%	-1740%
C_{Mx}	-34%	-53%	-50313%

Table 6.4 - Percentage change of single engine configurations w.r.t to WBTP

6.3 Considerations

Overall, in terms of longitudinal and lateral-directional stability and control, the two aircrafts have similar characteristics, differing only and minimally through the residual aerodynamic terms, with the Rutan Boomerang paradoxically being more stable than Cessna despite it being asymmetrical, although this fact strongly depends on the choice of the center of gravity. Hence it is safe to say that only in this specific choice of the centers of gravity, Boomerang is more stable than Cessna 402. The comparison between the coupling effects has been omitted since the difference between the two aircraft is minimal. On the other hand, a major difference is found in the propulsive effects: while the single engine configuration propulsive effects for the Boomerang are the same order of magnitude w.r.t. the both-engine-on configuration, for the Cessna it can be one or two. This reinforces the affirmation that Rutan Boomerang is less affected by the problem of asymmetric thrust encountered in conventional twin-engine aircraft.

Conclusion

This study shows that with the Open VSP software, it is possible to create and make a preliminary evaluation of innovative aircraft designs, such as the Rutan Boomerang, in an easy and rapid way. Due to its simplicity of use, coupled with the presence of a database of aircraft models, comparison with traditional aircraft designs is also possible. The results of the analysis give us a first answer to the question presented in the abstract. Despite the asymmetric and *bizarre* configuration of the aircraft, *"yes, that thing flies straight."* Nevertheless, the obtained data from the analysis should be compared and supported with data collected from wind tunnel testing and/or advanced CFD software. This can be done to further this research.

Bibliography

[1] Aerocrafted Engineering website: https://aerocrafted.com/

[2] Open VSP website: https://openvsp.org/

[3] J.D. Anderson Jr, *Fundamentals of aerodynamics*, 2nd ed., McGraw-Hill Inc, 1991.

[4] NASA, *Vortex-lattice utilization*. NASA SP-405, NASA-Langley, Washington, 1976.

[5] J. Katz, A. Plotkin, *Low-Speed Aerodynamics, 2nd ed., Cambridge University Press*, Cambridge, 2001.

[6] A. De Marco, D. Ciliberti, *Notes 05 – Equilibrium Flight.*

[7] VSP Airshow https://airshow.openvsp.org/

[8] SKYbrary website: https://skybrary.aero/aircraft/c402

Acknowledgements

This thesis was done with supervision of Prof. Danilo Ciliberti, that I personally thank for entrusting me with this challenging yet fulfilling project, that I really enjoyed working on. His guidance and support have been invaluable for the completion of this work, and I am truly grateful for his availability and the knowledge he shared with me through his insights.

I would like to dedicate this academic accomplishment to everyone who joined me through this wonderful journey, starting from those who nourished me through my whole life, who are my wonderful and hardworking parents: my mother Raissa and my father Brendo. I recognize that I am who I am molded by their unconditional love and support they give me day by day, rain or shine. This milestone is for all their sacrifices and the all the things they have endured to make sure that I receive quality education, and a peaceful and lovely home. I am deeply grateful for everything they have done for me, and I feel immensely lucky to have them as my parents.

To continue, I dedicate this achievement to my love Krizzia, who I met at the start of this chapter and accompanied me till the end, even though it has not been easy at all, due to the distance, the overlapping schedules and every other problem that relationships encounter. If there's someone who can depict and capture what I really have been through in these years, it's her. With her, every small victory felt the biggest, and every hardship felt like a small rock on the road. I would like to thank her for always believing in me even when I failed to do so. I'm truly grateful for having her by my side.

I would like to dedicate this work also to my siblings Raiven, Rovic and my fur sibling Althea for being such a supportive and sweet company at home. I am grateful for being your *kuya*.

A heartfelt thought and hug goes to the whole Bernardino family, firstly to my dearest *nanay* Ester, who took care of me when my parents could not, and to my supportive and generous uncles and aunts, in particular to my aunts Kelly and Thesz, and uncles Ryan, Ron, Rannie, Raffy and Carmelo for not failing to make their love be felt despite being on the other side of the world. I miss them all and I hope to see them soon.

A special appreciation goes to my childhood friends Nicole, Gerald and Malou, who have been there for me since forever, despite the distance. I thank them for their timeless friendship, and for the wonderful memories together.

I wish to acknowledge my *kuyas*, Jasper and Klein, who have been two reference points for my career. I would like to thank them for sharing their thoughts and judgement with me, that certainly helped me navigate the academic waters and further inspired me to pursue more knowledge.

I would also like to thank my friends Kim, Kate, Jhesus, Aaron, Tom and my high school classmates, for their friendship, the memories, the laughs, and their kindness towards me.

This journey would not have been as fun without my dear colleagues Alessio, Adelaide, Francesco and Angelo. I thank them for their pleasant company and for showing me their best skills and qualities, which pushed me to strive to be better not only academically but also as a person.

I then want to extend my gratitude to those who have been my educators, with a special mention to my piano teacher Rosa and to my *magister* Alfredo. I wholeheartedly thank them for teaching me how to make my soul resonate.

And last but not the least, I would like to thank God for the health, the qualities and the achievements he continuously lends me day by day.